

JGR Atmospheres

RESEARCH ARTICLE

10.1029/2021JD034876

Key Points:

- Northern Hemisphere wintertime polar front jet variability is associated with lower tropospheric baroclinicity anomalies
- Pacific tropical convection anomalies are linked to variations of the Northern Hemisphere wintertime subtropical jet at most longitudes
- Tropical convection in CMIP6 models is often displaced westward when compared to observations, reflecting a climatological bias

Supporting Information:

Supporting Information may be found in the online version of this article.

Correspondence to:

X. Liu,
x17pd@virginia.edu

Citation:

Liu, X., Grise, K. M., Schmidt, D. F., & Davis, R. E. (2021). Regional characteristics of variability in the Northern Hemisphere wintertime polar front jet and subtropical jet in observations and CMIP6 models. *Journal of Geophysical Research: Atmospheres*, 126, e2021JD034876. <https://doi.org/10.1029/2021JD034876>

Received 6 MAR 2021
Accepted 27 OCT 2021

Regional Characteristics of Variability in the Northern Hemisphere Wintertime Polar Front Jet and Subtropical Jet in Observations and CMIP6 Models

Xinhuiyu Liu¹ , Kevin M. Grise¹ , Daniel F. Schmidt¹ , and Robert E. Davis¹

¹Department of Environmental Sciences, University of Virginia, Charlottesville, VA, USA

Abstract Variability in the position and strength of the subtropical jet (STJ) and polar front jet (PFJ) streams has important implications for global and regional climate. Previous studies have related the position and strength of the STJ to tropical thermodynamic processes, whereas the position and strength of the PFJ are more associated with midlatitude eddies. These conclusions have largely resulted from studies using idealized models. In this study, ERA-Interim reanalysis and CMIP6 global climate models are used to examine month-to-month and interannual variability of the wintertime Northern Hemisphere (NH) STJ and PFJ. This study particularly focuses on the regional characteristics of the jet variability, extending previous studies on zonal-mean jet streams. Consistent with idealized modeling studies, a close relationship is found between tropical outgoing longwave radiation (OLR) and the STJ and between midlatitude lower tropospheric temperature gradients and the PFJ. Variations of both jets are also linked to well-known teleconnection patterns. Variations in tropical convection over the Pacific Ocean are associated with variations of the NH STJ at most longitudes, with different phases of the El Niño–Southern Oscillation (ENSO) associated with the shift and strengthening of the STJ in different regions. CMIP6 models generally capture these relationships, but the models’ tropical convection is often displaced westward when compared to observations, reflecting a climatological bias in OLR in the western tropical Pacific Ocean in many models. The displaced tropical convection in models excites different paths of Rossby wave propagation, resulting in different ENSO teleconnections on the STJ over North America and Europe.

1. Introduction

Jet streams are relatively narrow bands of strong west-to-east winds in the upper troposphere. In the zonal-mean climatology, there are two jet streams, the subtropical jet (STJ) and polar front jet (PFJ), located in both the Northern Hemisphere (NH) and Southern Hemisphere (SH). The STJ is commonly viewed as being driven by the angular momentum conservation in the poleward flowing upper tropospheric branch of the tropical Hadley circulation (Held & Hou, 1980; Schneider, 1977), and thus it is located near the poleward edge of Hadley Cell in each hemisphere. The PFJ is driven by the convergence of momentum by transient midlatitude eddies (Held, 1975; Panetta, 1993) and is consequently located at midlatitudes where baroclinic instability is strongest.

This simple picture of the two jet streams, however, does not apply at all longitudes and in all seasons. For example, in the NH wintertime climatology, there are clearly two distinct jets in Eurasia, the eastern Pacific Ocean, and the North Atlantic Ocean, while the STJ and PFJ are merged into a single jet stream in East Asia, the western Pacific Ocean, and the Eastern United States (Christenson et al., 2017; Eichelberger & Hartmann, 2007; Koch et al., 2006; Li & Wettstein, 2012). The strength of the two jets also varies by region, with both the STJ and PFJ usually strongest over the Pacific Ocean during winter (Archer & Caldeira, 2008; Koch et al., 2006). The NH jet streams are weaker and further poleward during summer months (Archer & Caldeira, 2008; Koch et al., 2006; Woollings et al., 2014). In the SH, a single jet stream is observed during summer, whereas somewhat more distinct STJ and PFJ are observed during winter (Bals-Elsholz et al., 2001; Kim & Lee, 2004).

The positions and strengths of the jets are not constant in time and vary from month to month and from year to year. Understanding variability in the position and strength of the jet streams is important, as it directly influences impactful surface weather events, such as extratropical cyclone tracks (Athanasiadis

et al., 2010; Dickson & Namias, 1976), blocking anticyclone frequency (Barnes & Hartmann, 2010; Kaas & Branstator, 1993; Woollings et al., 2018), heatwaves and cold air outbreaks (Mahlstein et al., 2012; Petoukhov et al., 2013), and atmospheric rivers and their associated heavy precipitation events (Ryoo et al., 2013; Zhang & Villarini, 2018). Previous studies have documented relationships between variability in the jet streams and known teleconnection patterns, including but not limited to the El Niño-Southern Oscillation (ENSO), the Northern Annular Mode (NAM)/North Atlantic Oscillation (NAO), the Pacific-North American teleconnection pattern (PNA), and the Southern Annular Mode (SAM). Variability in the PFJ is closely tied to the NAM/NAO, PNA, and SAM (Gallego et al., 2005; Strong & Davis, 2008; Woollings et al., 2010, 2014), whereas variability in the STJ is expected to correlate with ENSO (Gallego et al., 2005; Lu et al., 2008; Seager et al., 2003). Jet streams, of course, also vary with synoptic weather systems on daily time scales (Handlos & Martin, 2016; Winters & Martin, 2016), but in this study, we focus on month-to-month and interannual variability of the two jet streams.

Whether the STJ and PFJ are merged together or in two distinct branches may also have important implications for global and regional climate. One example is the relative minimum in North Pacific storm track activity that occurs during midwinter (January and February), even though the baroclinicity is the strongest during these months (Nakamura, 1992). A similar feature occurs in the North Atlantic storm track during years with a strong STJ (Afargan & Kaspi, 2017). Several recent studies have attributed the existence of a midwinter storm track minimum to the merging of the STJ and PFJ (Novak et al., 2020; Yuval et al., 2018). Previous studies have used idealized models to explain the merging and splitting of the two jets. Lee and Kim (2003) found that, when the STJ is relatively weak, the most favorable region for baroclinic wave growth often lies in midlatitudes, establishing an eddy-driven PFJ that is well separated from the STJ. In contrast, when the STJ is relatively strong, baroclinic wave growth occurs close enough to the STJ so that a single merged jet evolves. Son and Lee (2005) further found that a single merged jet forms preferentially when tropical heating is strong, while a double-jet state forms when tropical heating is weak enough to allow midlatitude eddies to grow more poleward and form a separate eddy-driven jet. Yuval and Kaspi (2018) concluded that baroclinic eddies are stronger when there is a strong distinct PFJ and are weaker when there is a merged jet.

These idealized model results provide insight into the processes that control the variability of the PFJ and STJ, but they are not entirely consistent with the jet characteristics found in observations or comprehensive global climate models. Based on the results of Lee and Kim (2003), one might expect that the positions and strengths of the STJ and PFJ are negatively correlated. That is, when the STJ is weak and equatorward, there should be a strong and poleward PFJ. However, several recent studies have found that interannual variability in the position and strength of the jets is only weakly correlated in the zonal-mean (Davis & Birner, 2016, 2017; Menzel et al., 2019; Solomon et al., 2016; Waugh et al., 2018). To our knowledge, apart from a recent study on the SH jets in the Indo-Pacific sector (Gillett et al., 2021), the relationship between the interannual variability in the position and strength of the jets has not been examined in detail at individual longitudes.

The purpose of this study is to better understand the month-to-month and interannual variability in the position and strength of the STJ and PFJ at individual longitudes. To do this, we define the position and strength of PFJ and STJ using both reanalysis data and global climate models. For this study, we focus our analysis on the wintertime (December–February) jets in the NH because longitudinal asymmetries are much greater in the NH and the jets are strongest in the winter season when the pole-to-equator temperature gradient is largest. We find that variations in (a) tropical convective heating and (b) horizontal lower tropospheric temperature gradients at midlatitudes are closely linked to the month-to-month and interannual variations in the position and intensity of the NH wintertime jet streams. Tropical convective heating is closely linked to variations in the location and strength of the NH wintertime STJ, consistent with the idealized modeling studies discussed above (Lee & Kim, 2003; Son & Lee, 2005), observations associated with the ENSO (Gallego et al., 2005; Lu et al., 2008), and case studies of synoptic-scale weather events (Handlos & Martin, 2016; Winters & Martin, 2016). Variations in lower tropospheric baroclinicity are closely linked to variations in the location and strength of the NH wintertime PFJ (see also Brayshaw et al., 2008; Hall et al., 2015; Sampe et al., 2010).

The study is organized as follows. Section 2 describes the data and methods used in this study. Section 3 examines the wintertime variability in STJ and PFJ position and strength in observations, and their linkages to tropical convective heating and midlatitude horizontal lower tropospheric temperature gradients. Section 4 explores the causes of model biases in these relationships. Section 5 concludes with a discussion and summary of the results.

2. Data and Methods

2.1. Data

To examine observed wintertime variability in the jets, we use monthly mean December–February zonal wind and 850 hPa temperature data from the European Centre for Medium-Range Weather Forecasts (ECMWF) Interim reanalysis data set (ERA-Interim; Dee et al., 2011). The data are provided at a spatial resolution of 0.75° latitude $\times 0.75^\circ$ longitude. We also make use of monthly mean outgoing longwave radiation (OLR) data from the National Oceanic and Atmospheric Administration (NOAA) interpolated OLR data set (Liebmann & Smith, 1996), which has a spatial resolution of 2.5° latitude $\times 2.5^\circ$ longitude. To quantify the relationships between the jet indices and several teleconnection patterns, we make use of monthly indices of the NAO and PNA from the National Weather Service Climate Prediction Center, and we use the monthly Niño 3.4 index (i.e., sea surface temperature anomalies averaged over 5°N – 5°S , 170° – 120°W) to represent ENSO. Our observational analysis is based on the 40-year period from January 1979 to December 2018, over which time we assume that there are 120 independent samples (3 months each for 40 years).

To compare the observed jet variability with that in global climate models, we examine output from the historical runs of 23 global climate models that participated in Phase 6 of the Coupled Model Intercomparison Project (CMIP6; Eyring et al., 2016), which are listed in Table S1 in Supporting Information S1. The historical runs of the models are designed to simulate the past climate over the period 1850–2014 by prescribing observed changes in radiative forcings (greenhouse gases, stratospheric and tropospheric ozone, tropospheric aerosols, volcanic eruptions, changes in solar output, etc.). We examine one ensemble member per model. The spatial resolution of the model output is highly variable and ranges from about 0.7° to about 2.8° (Table S1 in Supporting Information S1), so before analysis, all variables are interpolated to a common spatial resolution of 2.5° latitude $\times 2.5^\circ$ longitude. All of the model analyses are based on the 36-year period from 1979 to 2014, as the models' historical runs end in 2014. The observational analysis based on the 40-year period from 1979 to 2018 is very similar to that based on the 36-year period from 1979 to 2014 and thus can be directly compared to the model analyses in this study.

2.2. Methods

To define the position and strength of the PFJ and STJ, we exploit the fact that the STJ is defined by a baroclinic vertical structure (strong westerlies aloft and near-zero surface winds), whereas the PFJ is defined by an equivalent barotropic vertical structure (westerly wind maximum throughout the depth of the vertical column). Even though the wind speeds associated with both jets are maximized in the upper troposphere, it is challenging to uniquely identify the position and strength of each jet using the upper tropospheric wind field alone. Thus, following previous studies, we define the position and strength of the PFJ using the lower tropospheric wind field (e.g., Barnes & Polvani, 2013; Ceppi & Hartmann, 2013). Specifically, in this study, we define the position of the PFJ as the latitude of the maximum of the lower tropospheric (850 hPa) zonal wind averaged over a given longitude band between 20°N and 65°N . The location of maximum winds is determined by fitting a quadratic to the peak and finding the latitude of maximum wind speed at an interval of 0.01° (Barnes & Polvani, 2013). The strength of the PFJ is then determined using the value of the 850 hPa zonal wind at the identified PFJ position.

We define the position of the STJ as the latitude of the maximum value found in the difference field between the upper tropospheric (250 hPa) zonal wind and the lower tropospheric (850 hPa) zonal wind averaged over a given longitude band between 10° and 40°N . The lower tropospheric zonal wind is subtracted to isolate the vertically integrated thermal wind shear (Davis & Birner, 2016), as the STJ is defined by strong westerlies aloft and near-zero surface winds. In the zonal-mean, this method yields a comparable position to the NH STJ identified using tropopause height gradients (Maher et al., 2020). Following Menzel et al. (2019),

the strength of the STJ is then determined using the value of the difference field between the upper tropospheric (250 hPa) zonal wind and the lower tropospheric (850 hPa) zonal wind at the identified STJ position.

The above definitions of the jet streams have been used in a number of recent studies for zonal-mean diagnostics (Adam et al., 2018; Waugh et al., 2018). However, here we intend to apply these definitions both in the zonal-mean and at specific longitudes. To do this, we define regional jet indices, in which north-south zonal wind profiles are averaged over specific longitude bands prior to finding the jet positions and strengths. The six regions are defined as: Europe (0° – 50° E), Asia (50° E– 130° E), the western Pacific Ocean (130° E– 160° W), the eastern Pacific Ocean (160° W– 130° W), North America (130° W– 80° W), and the Atlantic Ocean (80° W– 0°). We also calculate the four jet indices (PFJ position, PFJ strength, STJ position, and STJ strength) at each individual longitude (i.e., using the north-south zonal wind profile at each longitude; see Figure 1).

3. Observed Variability in the Subtropical and Polar Front Jet Streams

We begin by reviewing the observed climatology of the NH wintertime jet positions and strengths. Figure 1 shows the NH wintertime (December–February) climatological positions (Figure 1a) and strengths (Figures 1b and 1c) of the PFJ and STJ along with their standard deviations at each longitude. In the NH wintertime climatology, there are clearly two distinct jets in Eurasia, the eastern Pacific Ocean, and the North Atlantic Ocean, while the STJ and PFJ are merged into a single jet stream in East Asia, the western Pacific Ocean, and the Eastern United States (Figure 1a), as also documented in previous studies (Christenson et al., 2017; Eichelberger & Hartmann, 2007; Koch et al., 2006; Li & Wettstein, 2012). The PFJ position has a similar standard deviation at most longitudes (6.73° latitude on average), with the largest standard deviations occurring over western Eurasia. In contrast, the standard deviation of the STJ position varies more substantially by longitude, with very small standard deviations (2.09° latitude) over Eurasia and the western Pacific Ocean and standard deviations comparable to that of the PFJ position at most other longitudes.

The strength of the two jets also varies by region. The strength of the PFJ (as measured by the 850 hPa zonal wind maximum) is largest (10–15 m/s zonal wind at 850 hPa) and displays the most variance over the storm track regions of the North Pacific and North Atlantic Oceans (Figure 1b). The strength of the STJ (as measured by the maximum of 250–850 hPa zonal wind difference) is largest (>40 m/s) over Eurasia and the western Pacific Ocean, with the largest wind speeds (>60 m/s) observed where the STJ and PFJ are merged over the western Pacific Ocean (Figure 1c). A small secondary peak in STJ strength is also observed in eastern North America where the two jets are merged. The standard deviation of the STJ strength varies little with longitude.

We next examine whether variability in the jet strengths and positions are correlated with one another, as could be anticipated from the results of Lee and Kim (2003). Figure 2 shows the correlations among the monthly time series of the positions and strengths of the STJ and PFJ. The correlations are shown for the zonal-mean (leftmost bar in each panel) and the six different regions defined in Section 2.2. The horizontal dashed lines in each panel indicate the minimum value for statistically significant correlations at the 95% confidence level.

With respect to the overall correlations between position and strength from the zonal-mean wind field, few statistically significant correlations are found, consistent with the results of Menzel et al. (2019). One exception is the significant negative correlation between the PFJ position and STJ strength (Figure 2b). In this case, a more poleward distinct PFJ is associated with a weaker STJ, as could be anticipated from the results of Lee and Kim (2003).

The weak correlations among the positions and strengths of the jets in the zonal-mean mask significant correlations among the positions and strengths of the jets that occur on the regional level, which highlights the need to examine the variability of the jets and the underlying mechanisms at individual longitudes. As in the zonal-mean (Davis & Birner, 2017; Menzel et al., 2019; Waugh et al., 2018), there are few significant correlations between the positions of the PFJ and STJ, except in the eastern Pacific and Atlantic sectors where a small negative relationship is observed (Figure 2a). Consistent with the results of Lee and Kim (2003), the PFJ position is negatively correlated with the STJ strength in the zonal-mean, and this negative correlation

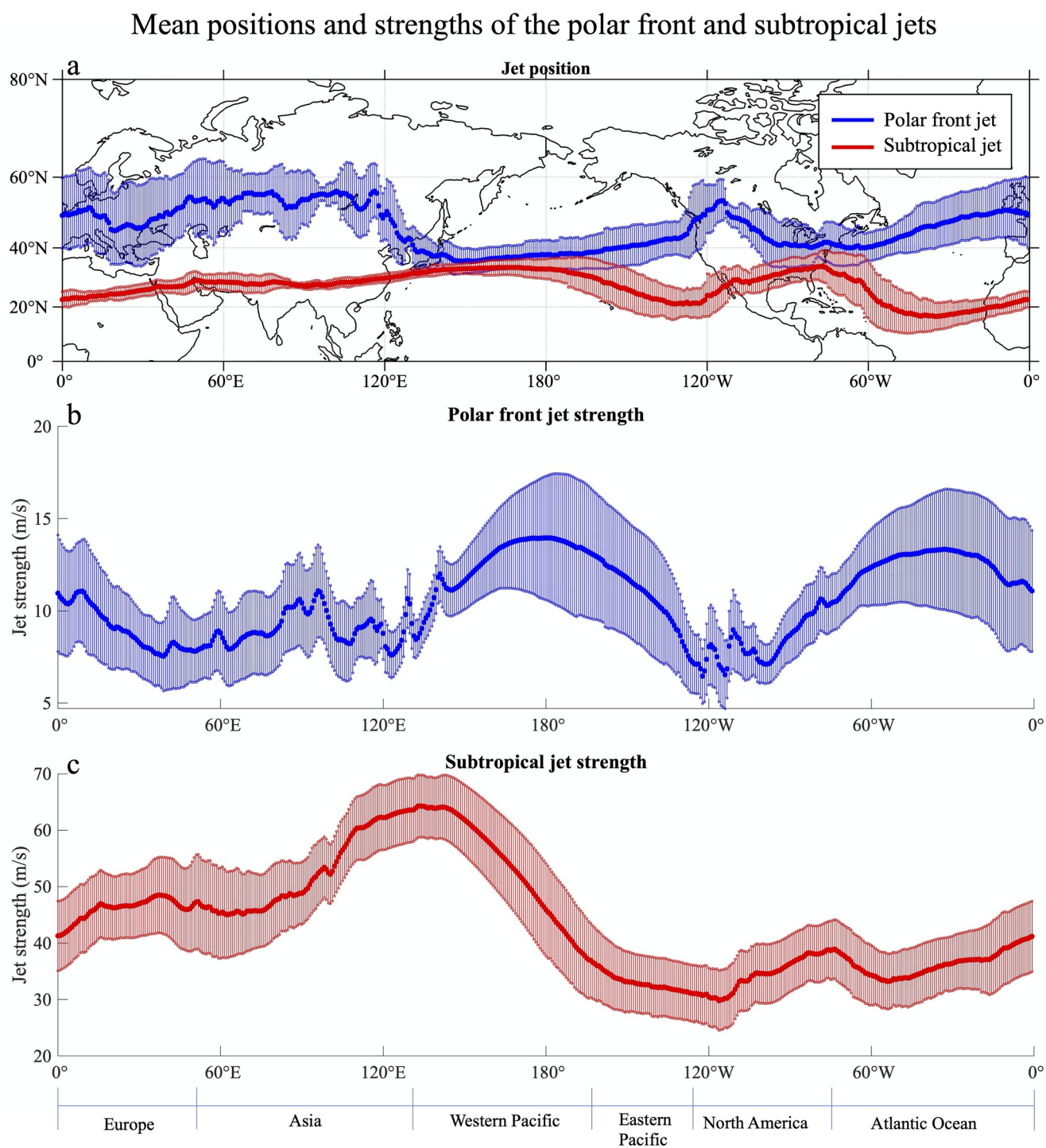


Figure 1. Mean positions (a) and strengths (b, c) of the Northern Hemisphere (NH) wintertime (December–February) PFJ and STJ with ± 1 standard deviation (shading) shown at all longitudes using jet indices derived from the ERA-Interim reanalysis data set from 1979 to 2018. Note that the jet strengths in panels (b) and (c) are plotted on different scales. The polar front jet is defined using the 850 hPa zonal wind, whereas the subtropical jet is defined using the 250–850 hPa difference in zonal winds.

arises predominantly from the western Pacific sector (Figure 2b). However, in other regions, the correlations are near-zero or of opposite sign. The strength and position of the PFJ are positively correlated over continents and negatively correlated over oceans (Figure 2c), whereas the strength and position of the STJ are positively correlated in Europe and the western Pacific and weakly correlated in other regions

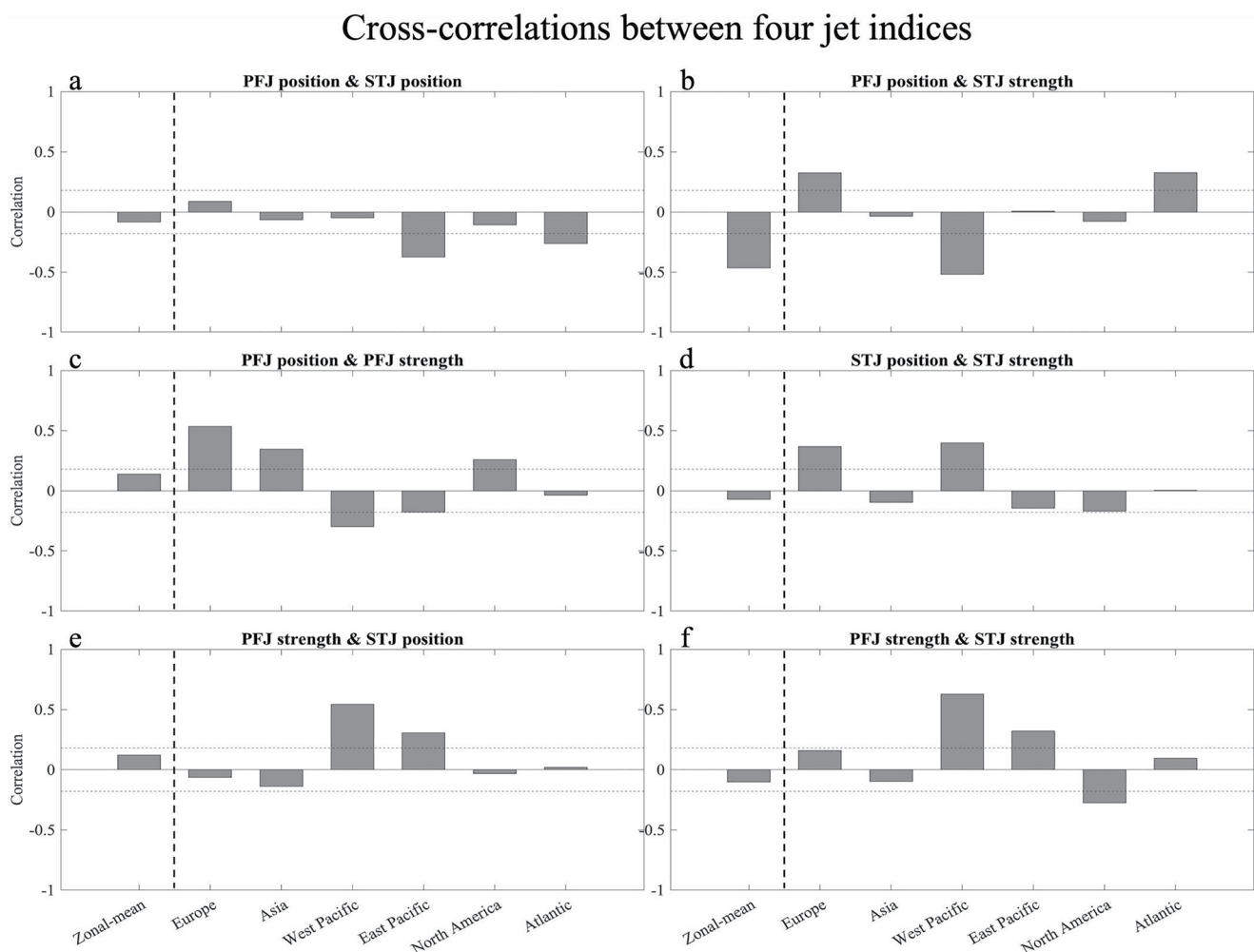


Figure 2. Correlations between monthly time series of the positions and strengths of the PFJ and STJ during NH winter, based on ERA-Interim reanalysis (1979–2018). The jets are defined in the zonal-mean and for the six different regions defined in Section 2.2. The seasonal cycle is removed prior to the analysis. The horizontal dashed lines in each panel indicate the minimum value for significant correlations at the 95% confidence level according to a two-tailed Student's *t* test.

(Figure 2d). Significant positive correlations also exist between the PFJ strength and STJ position/strength over the Pacific Ocean, particularly in the western Pacific where there is a merged jet (Figures 2e and 2f). We note that Gillett et al. (2021) recently documented significant negative correlations between SH PFJ position and STJ position in Indo-Pacific regions (consistent with the sign of the correlations in the eastern North Pacific and North Atlantic Oceans in Figure 2a), but significant negative correlations between SH PFJ strength and STJ strength in Indo-Pacific regions (in contrast to Figure 2f).

To interpret the correlations shown in Figure 2, we now examine the spatial patterns of temperature and OLR anomalies associated with variability in the positions and strengths of the jets. To do this, we regress monthly anomalies of OLR and 850 hPa temperature onto each of our four jet indices (PFJ position, PFJ strength, STJ position, and STJ strength) for NH winter months (i.e., the jet indices are 120 months for the 40-year ERA-Interim reanalysis record). Before the regression analysis, we remove the seasonal cycle of each time series by subtracting the monthly mean values from each month and normalize the jet indices by subtracting the mean and then dividing by the standard deviation. Results for the PFJ and STJ are shown in the following two subsections. We note that, in general, regressions on the distance between the two jets (i.e., the difference in the PFJ and STJ positions; not shown) closely resemble those associated with the PFJ position, which has a greater standard deviation at most longitudes (Figure 1a). Only over the eastern Pacific Ocean and Atlantic Ocean do regressions on the distance between the two jets also resemble those

Regression of 850 hPa temperature onto polar front jet position (observed)

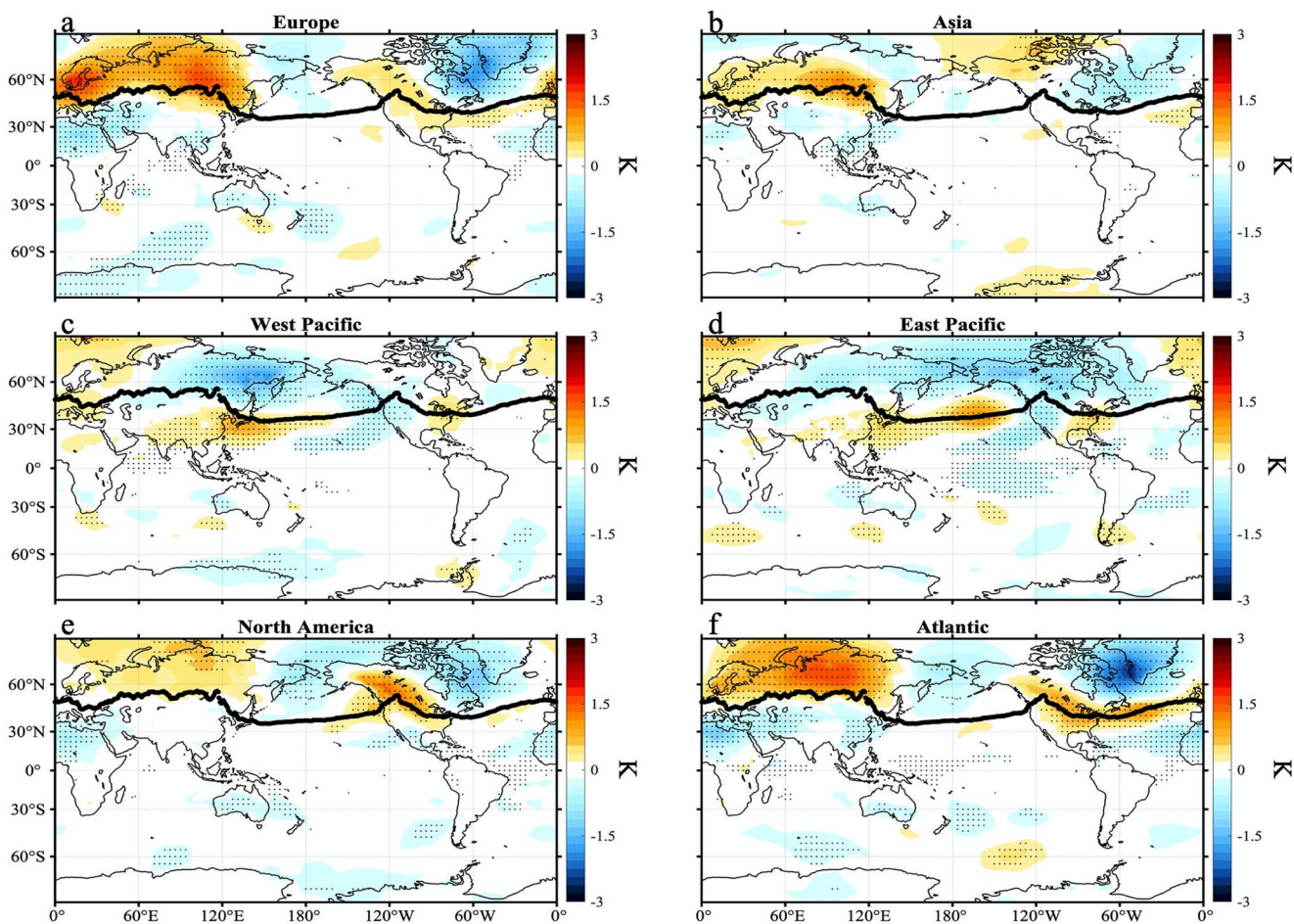


Figure 3. Regression of wintertime monthly 850 hPa temperature anomalies onto six different regions' polar front jet position in observations. Patterns correspond to 850 hPa temperature anomalies associated with a one standard deviation poleward shift of the PFJ in each region. Thick black lines on each panel are climatological PFJ positions in observations as shown in Figure 1a. Stippling indicates that regression patterns are statistically significant at the 95% level according to a two-tailed Student's *t* test. The model version of this figure is shown in Figure S1 in Supporting Information S1.

associated with the STJ position, suggesting that both the PFJ and STJ position play comparable roles in affecting the separation distance between the jets at these longitudes.

3.1. Polar Front Jet

Figure 3 shows the regressions of observed wintertime 850 hPa temperature anomalies onto the position of the PFJ in six regional sectors (as defined in Section 2.2). The 850 hPa temperature anomalies shown in each panel correspond to a one standard deviation poleward shift of the PFJ in each of the six regional sectors. Based on idealized aqua-planet simulations, we expect the location of the PFJ to be controlled closely by shifts in local baroclinicity (Brayshaw et al., 2008). Consistent with this expectation, we see a close correspondence in Figure 3 between temperature anomalies and the PFJ position in all regional sectors. Regressions of anomalies in the meridional temperature gradient at 850 hPa onto the position of the PFJ confirm that a poleward shift of the PFJ in these regions is associated with an increase in the local meridional temperature gradient to the north of the climatological PFJ position (see Figure 4).

The PFJ position is also closely linked to well-known global teleconnection patterns. For example, the temperature anomalies at 850 hPa associated with poleward shifts in the PFJ in the Atlantic, European, and

Regression of 850 hPa temperature gradient onto polar front jet position (observed)

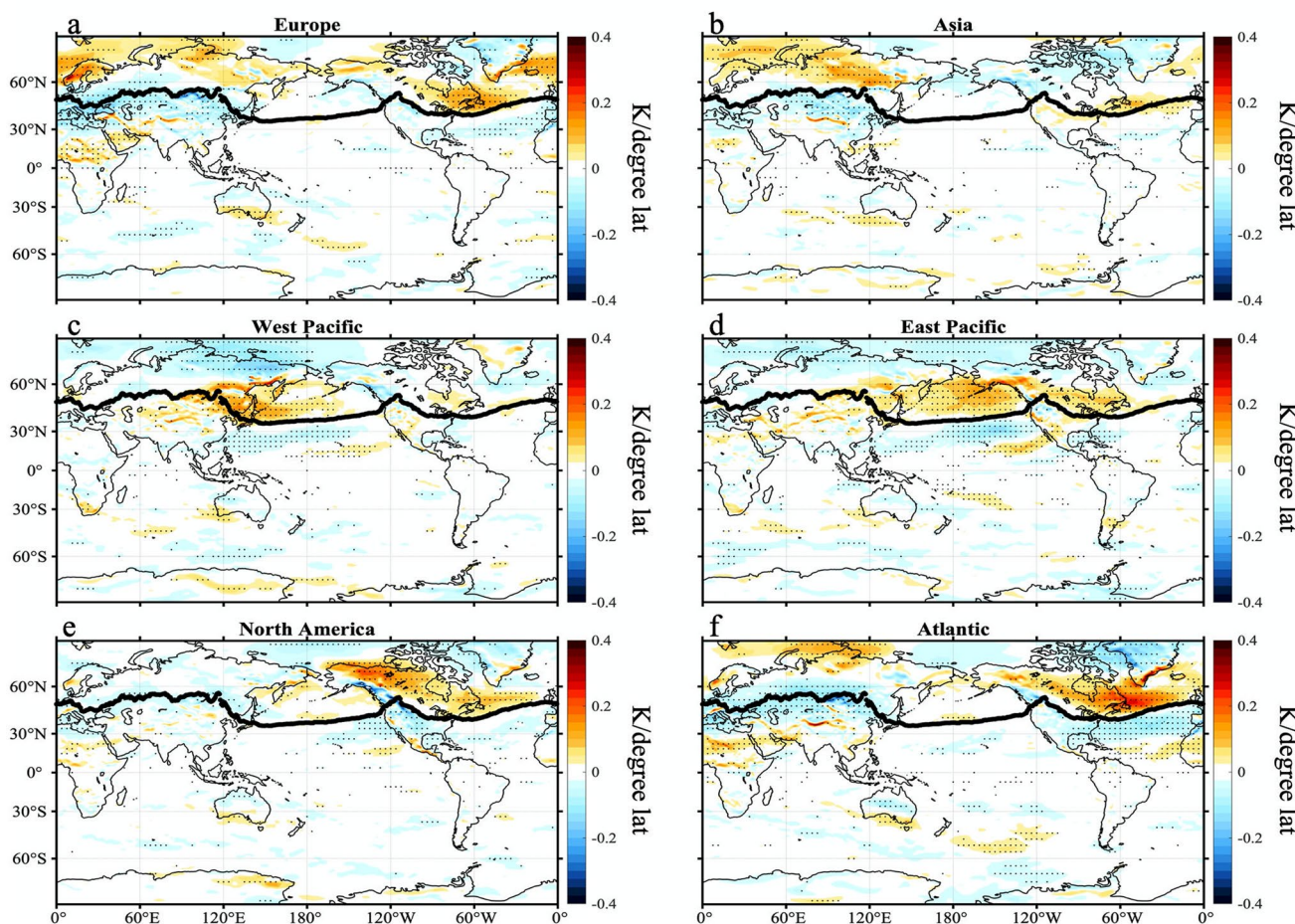


Figure 4. Regression of wintertime monthly 850 hPa meridional temperature gradient anomalies onto six different regions' polar front jet position in observations. Patterns correspond to 850 hPa meridional temperature gradient anomalies (K per degree latitude) associated with a one standard deviation poleward shift of the PFJ in each region. These 850 hPa meridional temperature gradient anomalies are calculated from south to north; therefore, red regions indicate an increase of the meridional temperature gradient. Thick black lines on each panel are climatological PFJ positions in observations as shown in Figure 1a. Stippling indicates that regression patterns are statistically significant at the 95% level according to a two-tailed Student's *t* test.

North American sectors closely resemble those associated with the positive phase of the NAO, which is characterized by above-normal temperatures over northern Europe and below-normal temperatures over Greenland and Eastern Canada (Hurrell, 1995). In the eastern Pacific sector, the temperature anomalies at 850 hPa associated with a poleward shift in the PFJ closely resemble those associated with the negative phase of the PNA (Wallace & Gutzler, 1981; Yu & Lin, 2019) and the cool phase of ENSO (Halpert & Ropelewski, 1992; Ropelewski & Halpert, 1989). A more detailed discussion about the linkages to the teleconnection patterns is provided below in Section 3.3.

Figure 5 shows analogous results to Figure 3, but for the PFJ strength. For reference, regressions of anomalies in 850 hPa meridional temperature gradient on PFJ strength are shown in Figure S3 in Supporting Information S1. The regression patterns of 850 hPa temperature anomalies onto PFJ strength (Figure 5) are similar to that of PFJ position (Figure 3) for Europe, Asia, and North America, but very different in the Pacific. This suggests that similar processes are associated with variations in PFJ position and intensity over the continents, but not necessarily over the oceans (see also Figure 2c). As for the PFJ strength in the Pacific sector, the temperature anomalies associated with PFJ intensification closely resemble those associated with the positive phase of PNA and the warm phase of the ENSO (Halpert & Ropelewski, 1992; Ropelewski & Halpert, 1989; Wallace & Gutzler, 1981; Yu & Lin, 2019). Intensification of the western and eastern Pacific

Regression of 850 hPa temperature onto polar front jet strength (observed)

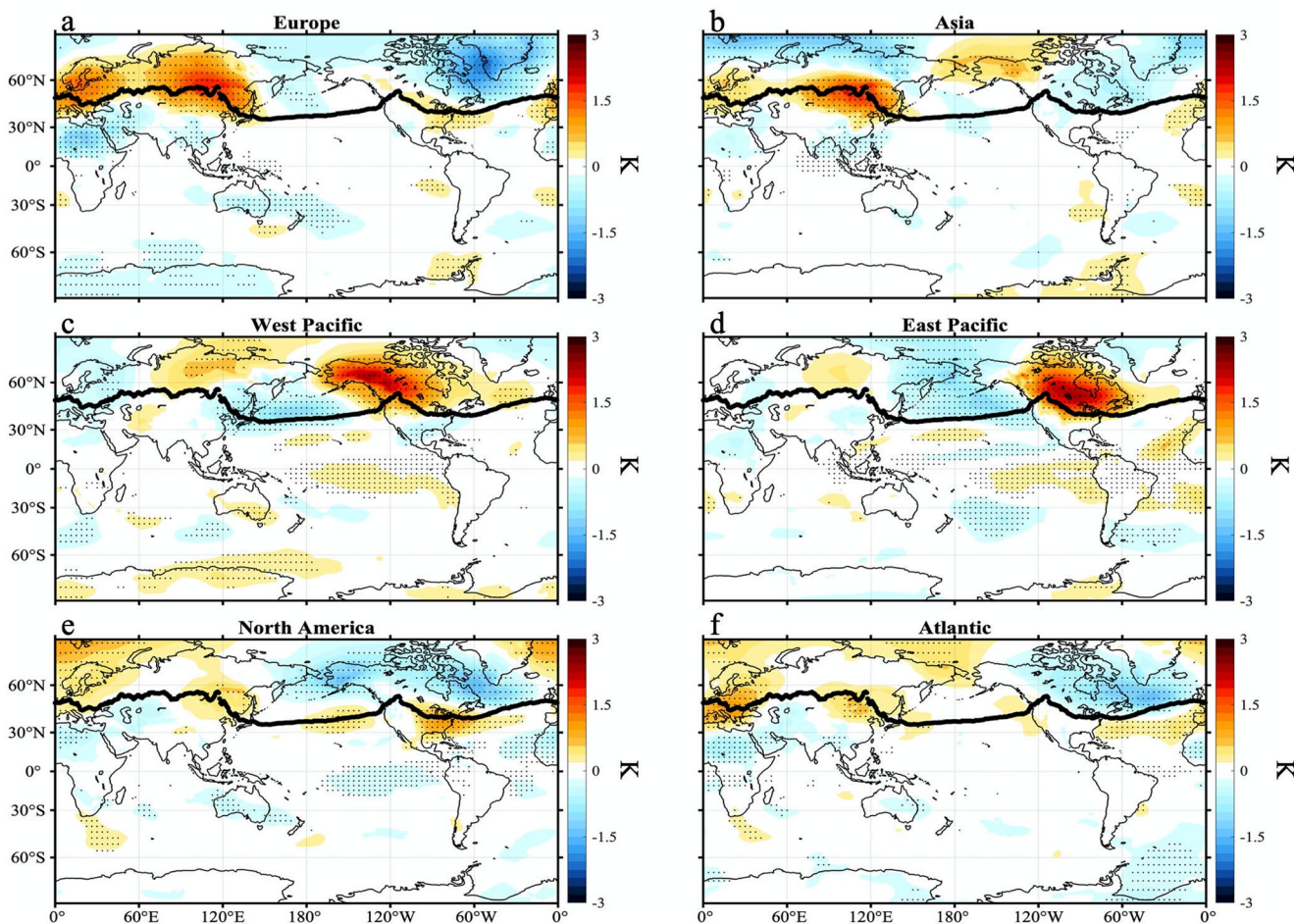


Figure 5. As in Figure 3, but for the PFJ strength. The model version of this figure is shown in Figure S2 in Supporting Information S1.

PFJ is associated with enhanced convection (anomalously low OLR) in the eastern tropical Pacific Ocean and suppressed convection (anomalously high OLR) in the western tropical Pacific Ocean (Figure S4 in Supporting Information S1). Alternatively, intensification of the North American PFJ is associated with the cool (La Niña) phase of ENSO (Figure S4 in Supporting Information S1). Intensification of the PFJ in other regions is not associated with significant variations in tropical convection (Figure S4 in Supporting Information S1), and variability in tropical convection also has little to no correlation with variability in PFJ position in any region except the eastern Pacific (not shown).

We note that the regression maps of 850 hPa temperature anomalies on the zonal-mean PFJ position closely resemble those of the Europe, Asia, North America, and Atlantic sectors (compare Figure S5a in Supporting Information S1 to Figure 3), whereas the regression maps of temperature anomalies at 850 hPa on the zonal-mean PFJ strength closely resemble those of the western and eastern Pacific Ocean sectors (compare Figure S5b in Supporting Information S1 to Figure 5). This is because the zonal-mean PFJ strength is dominated by the PFJ in Pacific where it is strongest (Figure 1b).

3.2. Subtropical Jet

Figures 6 and 7 show the regressions of observed wintertime OLR anomalies onto the position and strength of the STJ in six regional sectors (as defined in Section 2.2). The OLR anomalies shown in each panel correspond to a one standard deviation poleward shift (Figure 6) or strengthening (Figure 7) of the STJ in each of

Regression of OLR onto subtropical jet position (observed)

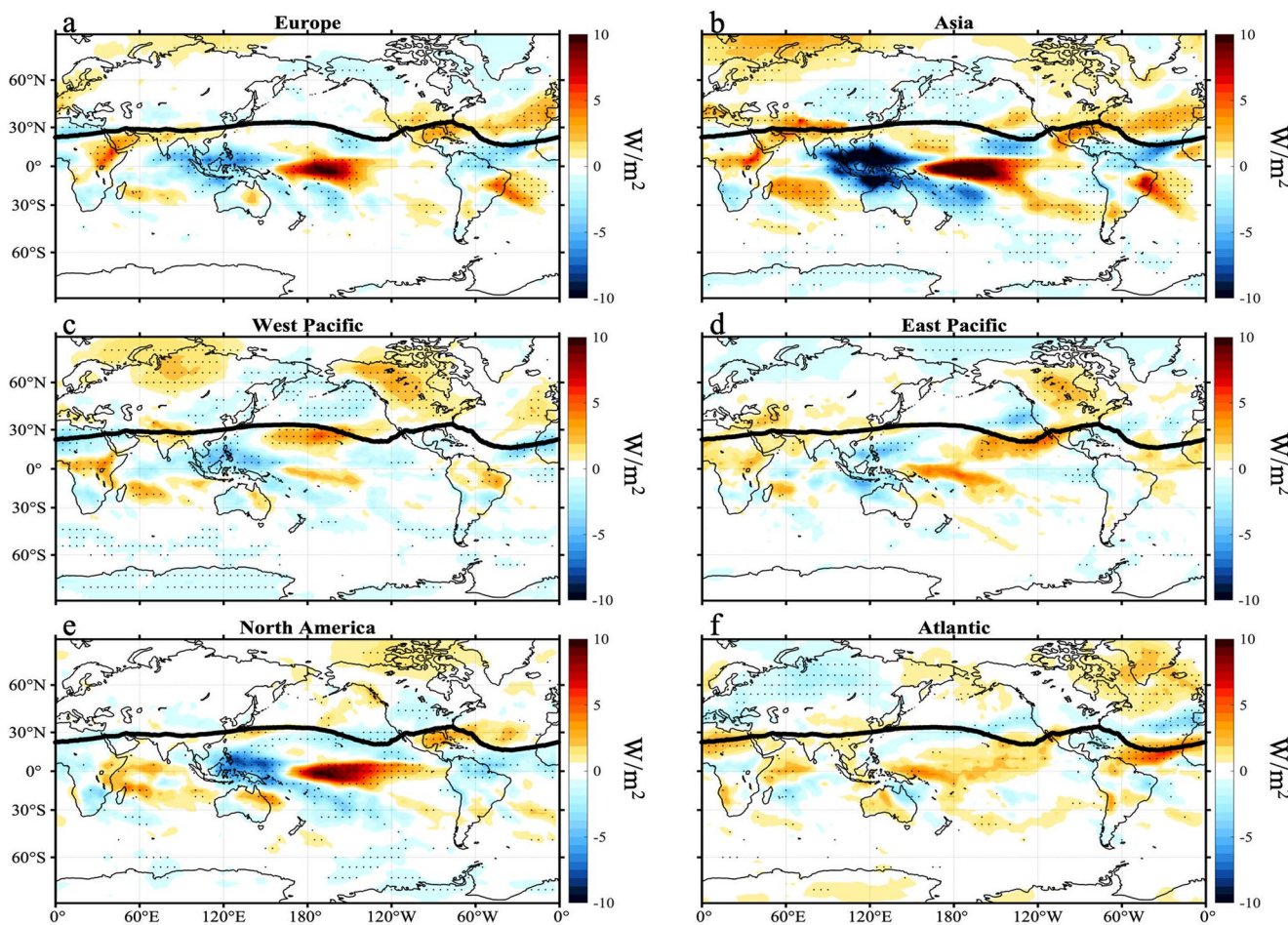


Figure 6. Regression of wintertime monthly outgoing longwave radiation (OLR) anomalies onto six different regions' subtropical jet position in observations. Patterns correspond to OLR anomalies associated with a one standard deviation of poleward shift of the STJ in each region. Thick black lines on each panel are climatological STJ positions in observations as shown in Figure 1a. Stippling indicates that regression patterns are statistically significant at the 95% level according to a two-tailed Student's *t* test. The model version of this figure is shown in Figure S8 in Supporting Information S1.

the six regional sectors. We also examined regressions of wintertime 850 hPa temperature anomalies onto the position and strength of the STJ (Figures S6 and S7 in Supporting Information S1), which highlighted relationships with well-known teleconnection patterns. We will discuss these linkages in Section 3.3.

Previous studies have concluded that tropical convection plays a critical role in forcing the position and strength of the STJ locally, particularly over the Pacific sector where El Niño is known to strongly modify the STJ (Gallego et al., 2005; Lu et al., 2008; Seager et al., 2003). Over the western Pacific, enhanced convection is associated with a strengthening and poleward shift of the STJ (Figures 6c and 7c), consistent with the idealized model results of Lee and Kim (2003) and Son and Lee (2005) and the correlation between western Pacific STJ position and strength in Figure 2d. Over the eastern Pacific, there is a robust relationship between enhanced convection (an El Niño-like pattern) and a strengthened STJ, but there is only a weak relationship between local convection and the STJ position (Figures 6d and 7d). Additionally, there is a robust relationship between a strengthened STJ over Asia and enhanced convection over the same longitude band (i.e., over the northern Indian Ocean). We note that the regression map of OLR anomalies on the zonal-mean STJ strength closely resembles that of the eastern Pacific Ocean sector (compare Figure S5d in Supporting Information S1 to Figure 7d).

Regression of OLR onto subtropical jet strength (observed)

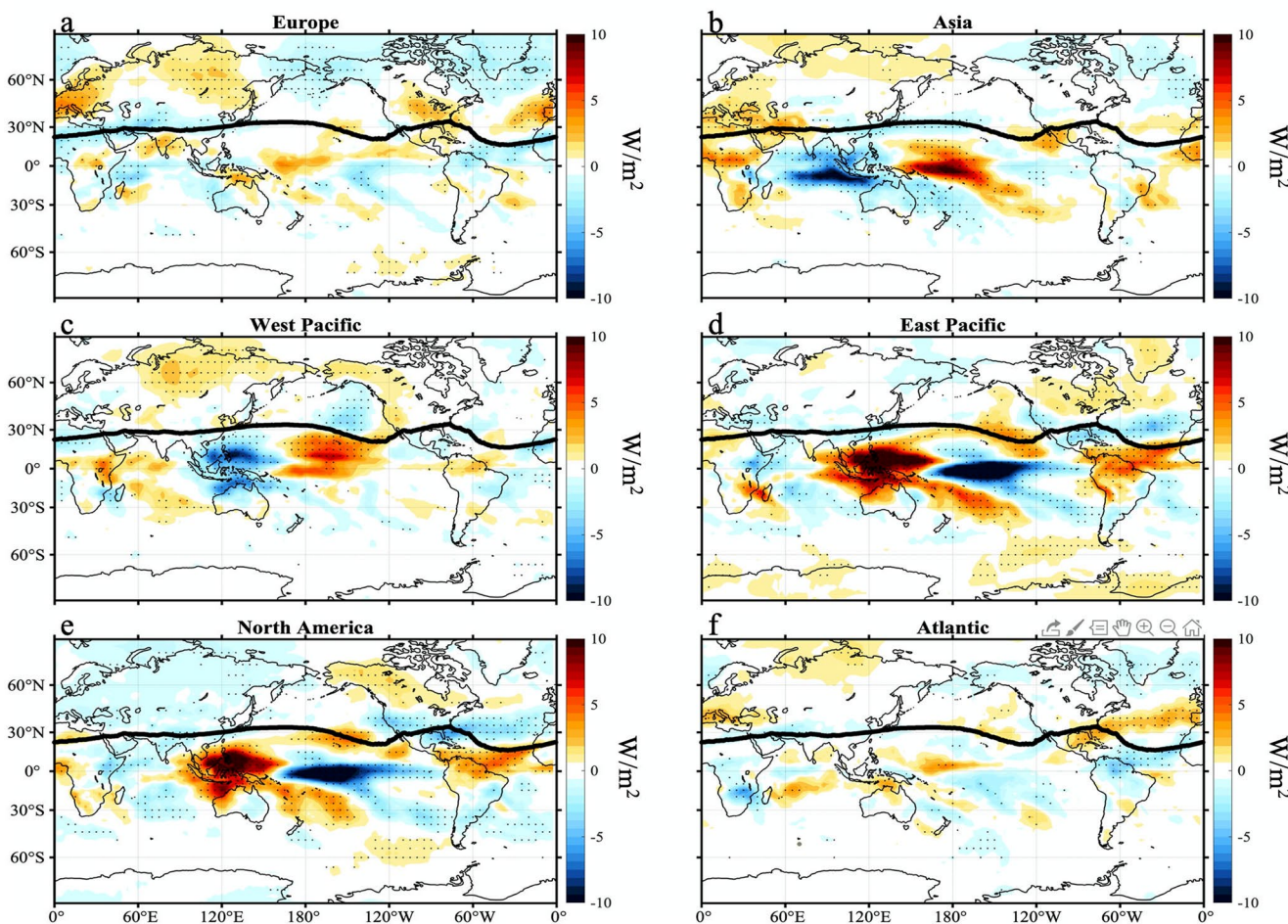


Figure 7. As in Figure 6, but for STJ strength. The model version of this figure is shown in Figure S9 in Supporting Information S1.

At most other longitudes, the variability in the STJ position and strength is more strongly linked to teleconnections from remote tropical convection anomalies over the Pacific basin than to tropical convection anomalies at the same longitude. We note that these relationships also exist when the tropical Pacific convection anomalies lead the variability in the STJ position and strength by 1 month (not shown). Figure 6 shows that a poleward shift of the STJ over Europe, Asia, and North America is associated with enhanced convection over western tropical Pacific Ocean (i.e., a La Niña-like pattern). A similar pattern of OLR anomalies is also found for regressions on the zonal-mean STJ position (Figure S5c in Supporting Information S1). The large influence of ENSO on the position of the North American STJ is consistent with the well-known teleconnections of ENSO over North America (Cook & Schaefer, 2008; Eichler & Higgins, 2006; Ropelewski & Halpert, 1989; Smith et al., 1998). As for the STJ strength, Figure 7 shows that enhanced convection in the eastern tropical Pacific Ocean (i.e., an El Niño-like pattern) is associated with a strengthened STJ over North America. Because enhanced convection in the western tropical Pacific Ocean is associated with a strengthened PFJ over North America (Figure S4 in Supporting Information S1), there is a negative correlation between PFJ and STJ strength over North America (Figure 2f).

To summarize these relationships, the left column of Figure 8 shows the regression coefficients of observed equatorial OLR anomalies onto indices of the STJ position and strength calculated at every longitude (as shown for the climatology in Figure 1). In other words, for each longitude on the y-axis in Figure 8, the horizontal line at that y-value shows the zonal cross section of tropical OLR anomalies at the Equator associated with STJ variability at that longitude. Figure 8 reveals that the STJ variability at nearly all longitudes is

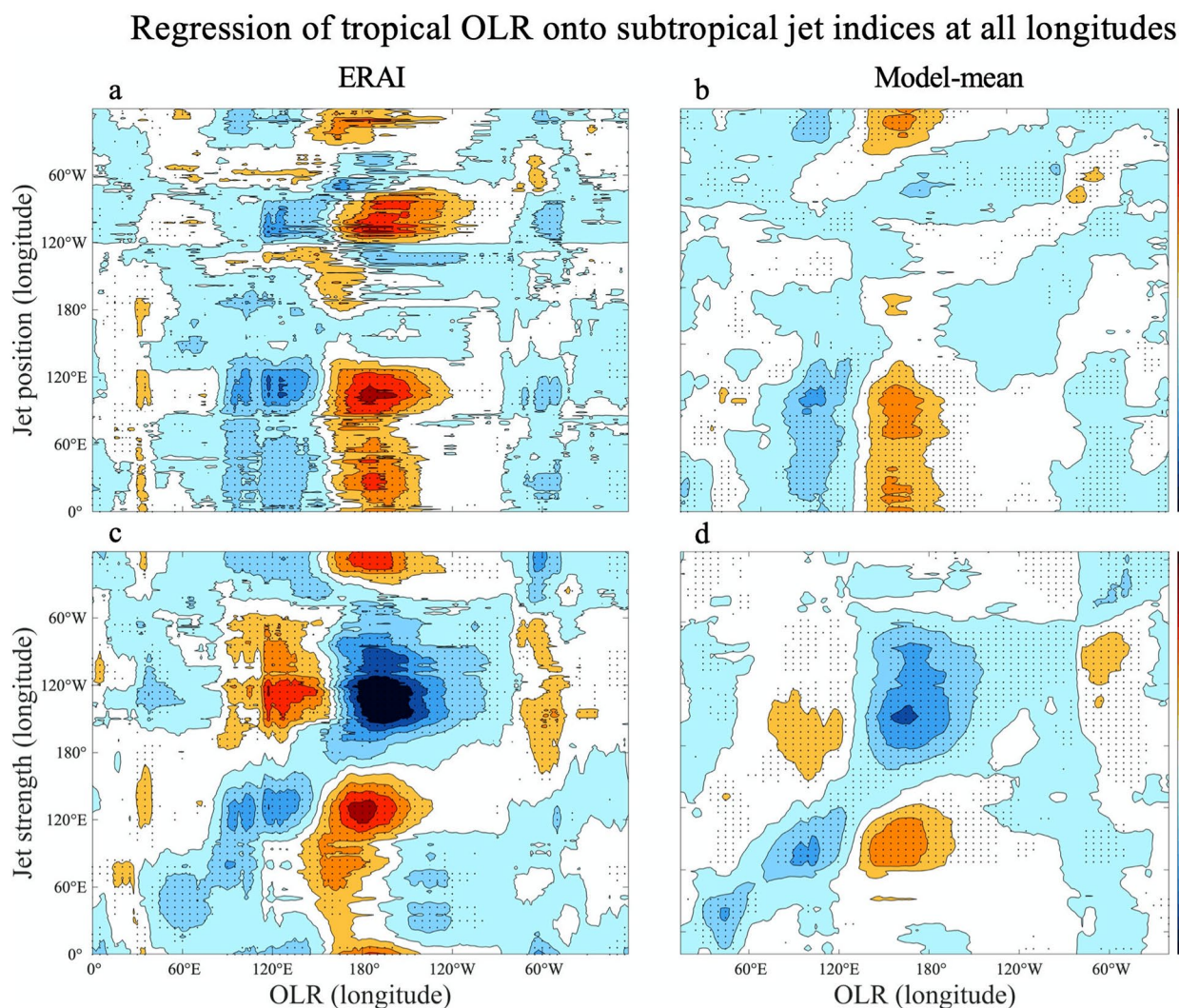


Figure 8. Regression of the wintertime monthly tropical OLR anomalies at the Equator onto subtropical jet indices at all longitudes. (a, b) Regression coefficients for subtropical jet position; (c, d) Regression coefficients for subtropical jet strength. The left column shows results for observations, and the right column shows results for the CMIP6 multimodel-mean. Color shading represents the regression coefficient of OLR at the longitude on the x-axis to the subtropical jet index at the longitude on y-axis. For panels (a) and (c), stippling indicates that regression patterns are statistically significant at the 95% level according to a two-tailed Student's *t* test. For panels (b) and (d), stippling indicates that more than 80% of models agree on the sign of the regression coefficients.

associated with a dipole of OLR anomalies over the tropical Pacific basin. This figure shows the dominance of ENSO (rather than local tropical convection) in governing STJ variability globally.

Consistent with Figure 6, Figure 8a reveals that a La Niña-like pattern of anomalous tropical convection is associated with a poleward shift of the STJ from the eastern Atlantic Ocean to the east coast of Asia, and over North America. Consistent with Figure 7, Figure 8c reveals that enhanced tropical convection from the western Indian Ocean to the eastern Pacific Ocean strengthens the STJ at that longitude, while enhanced tropical convection at other longitudes generally only has a weak relationship with the STJ strength at the same longitude. Looking across all longitudes, a La Niña-like pattern of anomalous tropical convection strengthens the STJ over the eastern Atlantic Ocean, western Europe, and the western Pacific Ocean, and an El Niño-like pattern of anomalous tropical convection strengthens the STJ over the eastern Pacific Ocean and North America (Seager et al., 2003).

Why do tropical convective anomalies strengthen the STJ locally in some longitudinal sectors but not others? We provide one hypothesis here. From the western Indian Ocean to the eastern Pacific Ocean, there is substantial tropical OLR variance relatively close to the STJ position (Figure 9a) during the DJF season, so it

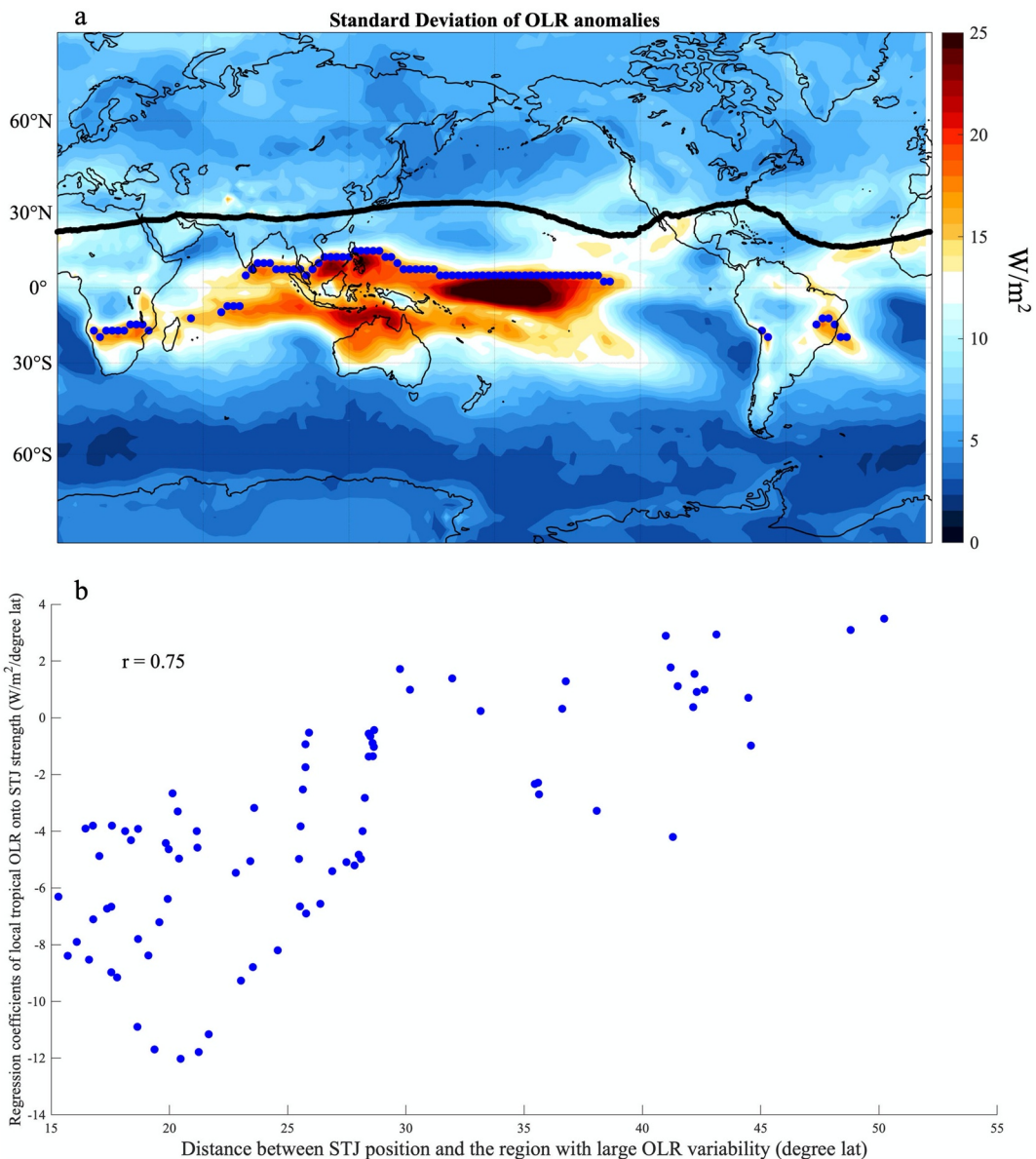


Figure 9. (a) Month-to-month standard deviation of OLR anomalies within DJF season (seasonal cycle removed). Thick black line is climatological STJ position in observations as shown in Figure 1a. The north boundary of the region with large OLR variability is defined as the first latitude where the standard deviation of OLR is greater than 16 W m^{-2} and is denoted as a blue dot at each longitude. (b) Scatter plot between the regression coefficients of local tropical OLR onto STJ strength (i.e., the values along the diagonal of Figure 8c) and the distances between STJ position and the region with large OLR variability across all longitudes in observations (i.e., distance between the black line and the blue dots at all longitudes).

seems likely that this OLR variability would strongly impact the STJ strength (via thermal wind balance to the associated upper tropospheric latent heating). However, over South America and Africa, the convection and OLR variability is well south of the equator and relatively far away from the NH STJ position during DJF (Figure 9a), which is consistent with tropical OLR variability at these longitudes playing less of a role in governing variability in STJ strength. To provide evidence for this hypothesis, Figure 9b shows the scatter plot between the regression coefficient of local tropical OLR onto STJ strength (i.e., the values along the diagonal of Figure 8c) and the distance between the climatological STJ position (Figure 9a, black line) and the region with large tropical OLR variability (standard deviation $> 16 \text{ W m}^{-2}$; Figure 9a, blue dots) at each longitude. The positive correlation ($r = 0.75$) supports the above speculation that in the regions where the

Table 1

Correlations Between NAO/PNA/Niño 3.4 Indices and PFJ Position/Strength in Six Regions and Zonal-Mean During NH Winter From 1979 to 2018

Correlations between PFJ indices and teleconnection patterns							
	Europe	Asia	West Pacific	East Pacific	North America	Atlantic	Zonal-mean
NAO and PFJ position	0.47	0.14	0.06	0.09	0.31	0.55	0.54
NAO and PFJ strength	0.47	0.07	-0.04	-0.04	0.44	0.43	0.00
PNA and PFJ position	0.12	0.05	-0.33	-0.45	0.16	0.03	-0.34
PNA and PFJ strength	-0.06	0.00	0.78	0.35	-0.26	-0.10	0.27
Niño 3.4 and PFJ position	0.00	-0.01	-0.04	-0.28	0.02	-0.03	-0.15
Niño 3.4 and PFJ strength	0.08	0.06	0.26	0.22	-0.20	0.03	0.22

Note. Bold numbers are statistically significant correlations at the 95% level according to a two-tailed Student's *t* test.

STJ position is located closer to large tropical OLR variability, the relationship between tropical OLR anomalies and STJ strength at the same longitude is more robust.

3.3. Correlations of Jet Indices With Teleconnection Patterns

To summarize the linkages between jet variability and teleconnection patterns, Tables 1 and 2 show the correlations between the wintertime monthly time series of three teleconnection patterns (NAO, PNA, and ENSO) and the wintertime monthly time series of the positions and intensities of the jets in each of the six regions, as well as the zonal-mean. Table 1 shows the correlations between the teleconnection indices and the PFJ position/strength, and Table 2 shows the same correlations but for the STJ position and strength.

As shown in Table 1, consistent with Figures 3 and 5, the positive phase of the NAO is significantly correlated with a poleward shift and a strengthening of the PFJ in the Europe, North America, and Atlantic sectors (Strong & Davis, 2008; Woollings et al., 2010). The positive phases of the PNA and ENSO are significantly correlated with an equatorward shift and strengthening of the PFJ in the Pacific Ocean and a weakening of the PFJ over North America (see also Figure S4 in Supporting Information S1).

For the STJ position and strength (Table 2), the positive phase of the NAO is significantly correlated with a poleward shift and a strengthening of the STJ in Eurasia and an equatorward shift and a strengthening of the STJ in the Atlantic. The positive phase of the NAO is also associated with a weakening of the STJ in the eastern Pacific and North America. These results are consistent with previous studies, which showed that the positive phase of the NAO is associated with separated jets in the Atlantic sector (Ambaum et al., 2001; Yuan et al., 2011) and a weakening of the STJ in the Pacific sector (Ambaum et al., 2001). The positive phase of the PNA is significantly correlated with a poleward shift and a strengthening of the STJ in the Pacific Ocean, particularly in the western Pacific (Strong & Davis, 2007), and an equatorward shift of the STJ in

Table 2

As in Table 1, but for STJ Position/Strength

Correlations between STJ indices and teleconnection patterns							
	Europe	Asia	West Pacific	East Pacific	North America	Atlantic	Zonal-mean
NAO and STJ position	0.22	0.30	0.19	-0.07	-0.02	-0.48	-0.14
NAO and STJ strength	0.35	0.20	0.02	-0.21	-0.21	0.21	-0.29
PNA and STJ position	-0.04	-0.07	0.53	0.23	-0.25	0.07	0.26
PNA and STJ strength	0.02	0.01	0.62	0.07	0.17	-0.23	0.39
Niño 3.4 and STJ position	-0.23	-0.42	-0.02	-0.03	-0.34	-0.07	-0.32
Niño 3.4 and STJ strength	-0.04	-0.13	-0.12	0.34	0.43	-0.16	0.33

Note. Bold numbers are statistically significant correlations at the 95% level according to a two-tailed Student's *t* test.

North America (Rodionov & Assel, 2001). Consistent with Figures 6 and 8a, La Niña (negative phase of ENSO) is associated with a poleward shift of STJ in Europe, Asia, and North America, and consistent with Figures 7 and 8c, El Niño (positive phase of ENSO) is associated with a strengthened STJ over the eastern Pacific Ocean and North America. We note that the correlations between Niño 3.4 index and STJ position/strength are stronger with a 1-month lead of Niño 3.4 index (not shown).

The correlations between the teleconnection indices and the zonal-mean jets generally mirror the behavior of the jets in the longitude bands with the largest correlations (see also Figure S5 in Supporting Information S1). One exception is the relationship between NAO and PFJ strength. Even though there are strong correlations between the NAO and PFJ strength in the Europe, North America, and Atlantic sectors, the correlation between the NAO and the zonal-mean PFJ strength is very small. This is because the zonal-mean PFJ strength is dominated by the PFJ in Pacific where it is strongest (Figure 1b).

4. Comparison Between Models and Observations

In this section, we compare the observed variability in the position and strength of the jets (as documented in Section 3) with that from CMIP6 models. To do this, we make use of multimodel-mean regression maps to summarize the average behavior of CMIP6 models. These maps are calculated as follows. First, the regression maps are calculated individually for each of the 23 CMIP6 models using the wintertime monthly variability of each model over the period 1979–2014 (as shown for the observations in Figures 3 and 5–7). Then, these 23 maps are averaged together to show the multimodel-mean pattern of 850 hPa temperature and OLR anomalies associated with wintertime jet variability. Note that, if instead we averaged the jet indices and 850 hPa temperature and OLR anomalies from each model together before performing the regression, we would average out the internal variability that is the focus of this study.

Model results for the regressions on PFJ position and strength are shown in Figures S1 and S2 in Supporting Information S1, and model results for the regressions on STJ position and strength are shown in Figures S8 and S9 in Supporting Information S1. The model regressions of 850 hPa temperature anomalies onto the PFJ position and strength are very similar to those shown for observations (Figures 3 and 5), but the model regressions of OLR anomalies onto STJ position and strength differ significantly from observations (Figures 6 and 7). For that reason, in this section, we focus on the comparison of the STJ variability between observations and CMIP6 models.

To summarize the model biases in STJ variability, the right column of Figure 8 shows the CMIP6 multimodel-mean regression coefficients of equatorial OLR anomalies onto indices of the STJ position and strength calculated at every longitude (as shown in the left column for observations). Consistent with observations (Figures 6 and 7), it is worth noting that the STJ at each longitude in the multimodel-mean is not primarily associated with OLR anomalies at its own longitude, but rather is linked to tropical OLR anomalies in the Pacific. However, for the OLR anomalies associated with a poleward shift in the STJ, tropical convection in the models is displaced westward over Eurasia when compared to observations (Figures 8a and 8b). Additionally, large discrepancies between the observed and model patterns occur in the North America. Over North America in observations, a La Niña-like pattern in anomalous tropical convection is associated with a poleward shift of the STJ position, but this pattern is not shown in models. For the OLR anomalies associated with a strengthening of the STJ (Figures 8c and 8d), most models capture the observed relationship between La Niña and a strengthened STJ over the western Pacific Ocean and between El Niño and a strengthened STJ over the eastern Pacific Ocean and North America (see the prominent quadrupole pattern in the left-center of panels c and d). However, most models fail to capture the observed relationship between tropical convection and the STJ strength over the eastern Atlantic Ocean and Eurasia.

We now discuss the possible causes of these model-observation discrepancies shown in Figure 8. As discussed above, models agree that a La Niña-like pattern in anomalous tropical convection is associated with a poleward shift of the STJ position over Eurasia, but the dipole of OLR anomalies is shifted to the west in the multimodel-mean compared to observations (Figures 8a and 8b). To illustrate this more clearly, the top row of Figure 10 shows the regressions of OLR anomalies onto the STJ position in the Asian sector (as shown in Figure 6 and Figure S8 in Supporting Information S1, but zoomed in to show greater detail). In particular, notice that the region of enhanced convection in the multimodel-mean is narrower and confined

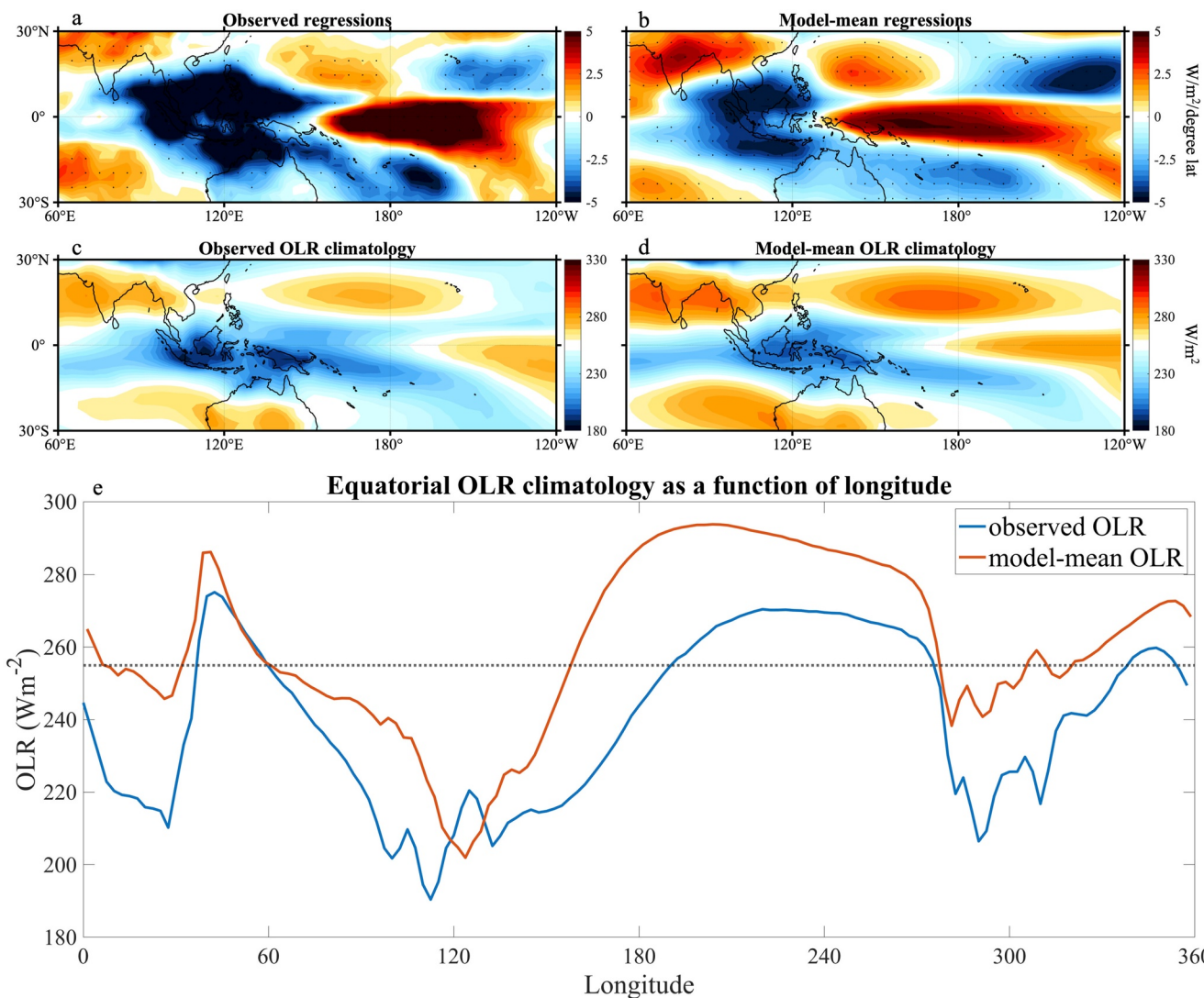


Figure 10. (a, b) Regressions of monthly wintertime OLR anomalies to the Asian STJ position for observations and the CMIP6 multimodel-mean (reproduced from the second panels of Figure 6 and Figure S8 in Supporting Information S1 but zoomed in and with different color scales). (c, d) The wintertime OLR climatology for observations and the CMIP6 multimodel-mean. (e) The observed and multimodel-mean wintertime OLR climatology at the Equator as a function of longitude. The blue line shows the observed OLR, while the red line shows the model-mean OLR. The dashed black line shows the 255 W m^{-2} OLR value, below which is defined as low OLR.

to longitudes west of the Philippines and that the region of suppressed convection along the Equator in the multimodel-mean extends much further to the west over New Guinea (Figure 10b).

One reason for the westward shift of the La Niña-like pattern in models could be that the climatological OLR field in CMIP6 models is different from that in observations, as some previous studies have documented that ENSO diversity is associated with the tropical Pacific background state (Capotondi et al., 2015; Choi et al., 2011; Chung & Li, 2013). The observed and multimodel-mean OLR climatology in the equatorial Pacific is shown in Figures 10c and 10d. The equatorial low OLR region in observations in the western Pacific is wider and extends further eastward than in the multimodel-mean climatology, which is consistent with previous findings that many climate models simulate an excessive westward extension of the cold tongue into the tropical Pacific warm pool (Ding et al., 2020; Li & Xie, 2014; Lin, 2007). To illustrate this better, we also plot the cross section of observed and multimodel-mean climatological OLR at the Equator as a function of longitude in Figure 10e.

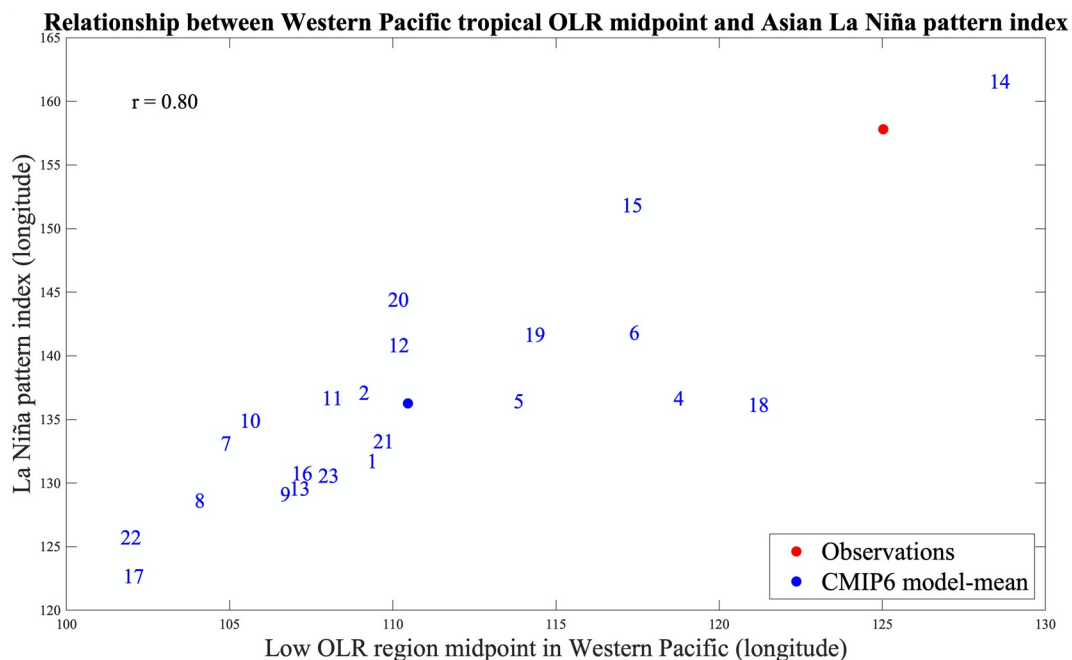


Figure 11. Scatter plot between the midpoint of the wintertime climatological low OLR region over the western Pacific and the La Niña pattern index. The La Niña pattern index is defined as the transition longitude between 120°E and 180°E where the regression coefficient of wintertime monthly OLR anomalies to the Asian STJ position (as shown in Figures 10a and 10b) averaged over 10°S–20°N crosses zero. The midpoint of the climatological low OLR region is defined as the midpoint longitude of the low OLR region in equatorial western Pacific (as shown in Figure 10e). The low OLR region is defined where the OLR is smaller than 255 W m^{-2} . Numbers on the scatterplot correspond to the models listed in Table S1 in Supporting Information S1. The blue dot represents multimodel-mean, while the red dot is for observations.

In Figure 11, we show the correlation between the position of the climatological low OLR region along the Equator in the western Pacific Ocean (as shown in Figure 10e) and the position of the OLR anomalies associated with a poleward STJ shift over the Asia sector (as shown in Figures 10a and 10b) across CMIP6 models. The climatological low OLR region is defined as the region where OLR is smaller than 255 W m^{-2} , and we define the position of the low OLR region as the midpoint longitude of the low OLR region in the equatorial western Pacific. The results are not sensitive to the exact choice of threshold value (i.e., values between 250 and 270 W m^{-2} give similar results). The position of the OLR associated with a poleward STJ shift over the Asia sector, which we refer to as the “La Niña pattern index,” is defined as the transition longitude between 120° and 180°E where the regression coefficient of OLR to Asian STJ position (as shown in Figures 10a and 10b) averaged over 10°S–20°N crosses zero. The positive relationship between the midpoint of the climatological low OLR region and the La Niña pattern index ($r = 0.80$) indicates that the westward La Niña-like pattern in models’ tropical convection associated with a poleward STJ shift over the Eurasian sector can be attributed to the biased OLR climatology in the tropical western Pacific Ocean in many models. The western Pacific tropical convection is centered further to the west than observations in nearly all of the models and thus causes a westward shift of the La Niña-like pattern of anomalous tropical convection.

Another key discrepancy between observations and models shown in Figure 8 is that models fail to capture the linkage between a La Niña-like pattern of anomalous tropical convection and the poleward shift of the STJ over North America (Figure 8b). Given the biased OLR climatology in models, it seems plausible that different Rossby wave trains would be excited by tropical convection at different locations associated with El Niño and La Niña patterns in observations and models (Jiménez-Esteve & Domeisen, 2018). To illustrate this, Figure 12 shows the regressions of 500 hPa eddy geopotential height anomalies and anomalies in the 250–850 hPa zonal wind difference field (i.e., the field used to calculate the STJ position; see Section 2.2) onto the Niño 3.4 index for both observations and the CMIP6 multimodel-mean. Here, the term eddy geopotential height anomalies means that both the zonal-mean and seasonal cycle have been removed from the

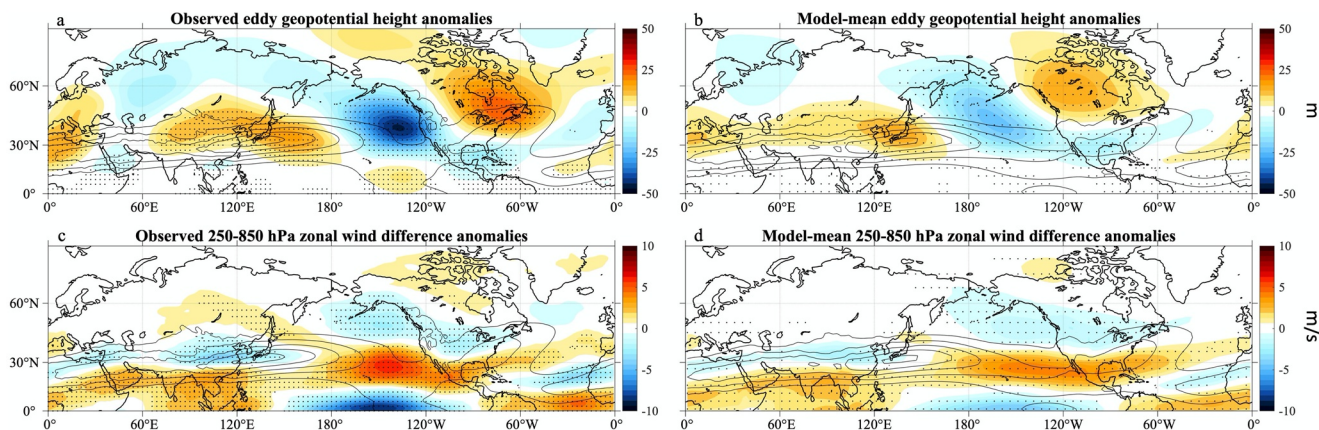


Figure 12. Regression of wintertime monthly eddy 500 hPa geopotential height anomalies (i.e., with both the seasonal cycle and zonal-mean field removed) and 250–850 hPa zonal wind difference anomalies onto the Niño 3.4 index in observations (a, c) and the CMIP6 multimodel-mean panels (b, d). Stippling in panels (a) and (c) indicates that regression patterns are statistically significant at the 95% level according to a two-tailed Student's *t* test, and stippling in panels (b) and (d) indicates that more than 80% of models agree with the sign of regression coefficients. Black contours indicate the climatology of zonal wind difference field (250 hPa zonal wind–850 hPa zonal wind), which is used to define the STJ position. Contours are shown at 20, 30, 40, 50, and 60 m/s.

geopotential height data. As shown in Figure 12a, the wave train excited by anomalous tropical convection in observations is further south and east compared to that in multimodel-mean. Consequently, a north-south dipole of eddy geopotential height anomalies and a north-south dipole of zonal wind anomalies are located directly over the STJ in eastern North America in observations, but not in models.

Finally, we noted above that models fail to capture the observed relationship between a La Niña-like pattern of anomalous tropical convection and STJ strength over the eastern Atlantic and European sectors (Figure 8d). As shown in Figure 12a, the wave train associated with ENSO in observations propagates poleward to Alaska and Canada and then back equatorward toward the North Atlantic and Western Europe, where it projects onto the STJ in this region. In the multimodel-mean, the wave train associated with ENSO is shifted further westward and thus returns equatorward over the central Atlantic Ocean (Figure 12b). However, ENSO's impacts in the North Atlantic may be highly variable and unstable (note lack of significance in Figures 12a and 12b over North Atlantic), which means that the observed teleconnections in this sector may be highly sensitive to the time frame we choose (Greatbatch et al., 2004).

5. Summary and Conclusions

The position and intensity of the PFJ and STJ streams in NH winter exhibit large spatial and temporal variance. Some previous studies (e.g., Lee & Kim, 2003; Son & Lee, 2005) have provided insight into the processes that control the variability of the PFJ and STJ, but most of these studies have relied on idealized aqua-planet models with no zonal asymmetries in the jets. Although correlations among variations in the strength and position of the jets could be anticipated from such idealized modeling studies, variability in the position and strength of the zonal-mean STJ and PFJ actually exhibits few significant correlations in observations and comprehensive global climate models (Figure 2; Davis & Birner, 2017; Menzel et al., 2019; Solomon et al., 2016; Waugh et al., 2018). The lack of significant correlations among the position and strength of the jets in the zonal-mean masks significant correlations among those of the jets that occur on the regional level (see also Gillett et al., 2021), particularly in the Pacific regions (Figure 2), which highlights the need to examine the month-to-month and interannual variability of the jets and their possible underlying mechanisms at individual longitudes.

In this study, we find a close relationship between the observed variability in the position and strength of the STJ and tropical OLR and between the observed variability in position and strength of the PFJ with midlatitude temperature gradients during the NH winter season. In many regions, the variability in the positions and strengths of the jets is closely linked to well-known global-scale teleconnection patterns, such as the NAO, PNA, and ENSO (Tables 1 and 2). Local changes in lower tropospheric baroclinicity are associated

with variability in the position and strength of the NH PFJ at all longitudes (Figure 4). Variations in tropical convection over the Pacific Ocean are linked to variations in the strength and position of the NH STJ at almost all longitudes, with different phases of the ENSO associated with the poleward shift and strengthening of the STJ in different regions (Figures 6 and 7).

CMIP6 models generally capture these observed relationships, but for the STJ variability, the models' tropical convection is often displaced westward when compared to observations (Figures 8 and 10). This difference between models and observations can be attributed to the biased OLR climatology over the tropical western Pacific Ocean in many models, with climatological convection in models displaced westward with respect to observations (Figures 10 and 11). The displaced tropical convection in models excites different paths of Rossby wave propagation, making downstream ENSO teleconnections on the STJ over North America, the Atlantic Ocean, and Europe different compared to observations (Figure 12).

Our study examines observed characteristics of the NH wintertime STJ and PFJ at all longitudes and provides insight into the processes governing their month-to-month and interannual variability over the last four decades. Future work could extend this study to the SH (expanding the results of Gillett et al., 2021 to all longitudes) or investigate the jet variability in other seasons in the NH. It may also be worthwhile to examine whether the relationships documented here change in the future as the climate warms. Although climate models show a robust poleward shift of the PFJ in a warming climate (e.g., Barnes & Polvani, 2013), the STJ does not show a consistent poleward or equatorward shift, at least in the zonal-mean (Davis & Birner, 2017; Menzel et al., 2019; Waugh et al., 2018). Recent reanalysis data also show poleward trends in the PFJ position (e.g., Allen & Kovilakam, 2017; Grise et al., 2018), but inconsistent trends in the STJ position (Maher et al., 2020; Manney & Hegglin, 2018). Not only does this suggest that the mechanisms driving the responses of the STJ and PFJ to climate change could be very different (as discussed by Menzel et al., 2019), but it also implies that the character of the general circulation (i.e., preference for a merged jet at some longitudes and two distinct jets at other longitudes) may change as the climate warms, hence modulating month-to-month and interannual variability of the jets and the associated behavior of synoptic weather events.

Data Availability Statement

CMIP6 model output is freely available from the Lawrence Livermore National Laboratory (<https://esgf-node.llnl.gov/search/cmip6/>). ERA-Interim reanalysis data are freely available from the European Centre for Medium-Range Weather Forecasts (<https://apps.ecmwf.int/datasets/data/interim-full-mod4/>; <https://cds.climate.copernicus.eu/#/search?text=ERA5&type=dataset>). Monthly outgoing longwave radiation (OLR) data sets are freely available from NOAA Physical Sciences Laboratory (https://psl.noaa.gov/data/gridded/data.interp_OLR.html). Monthly indices of NAO and PNA are freely available from the National Weather Service Climate Prediction Center (https://www.cpc.ncep.noaa.gov/products/MD_index.php).

Acknowledgments

The authors thank three anonymous reviewers for constructive comments. The authors acknowledge the World Climate Research Programme, which, through its Working Group on Coupled Modelling, coordinated and promoted CMIP6. The authors thank the climate modeling groups for producing and making available their model output, the Earth System Grid Federation (ESGF) for archiving the data and providing access, and the multiple funding agencies who support CMIP6 and ESGF. The authors also thank Carlee Kleppin (University of Virginia) for her initial work on this topic. This material is based in part upon work supported by the National Science Foundation under grant no. AGS-1752900.

References

- Adam, O., Grise, K. M., Staten, P., Simpson, I. R., Davis, S. M., Davis, N. A., et al. (2018). The TropD software package (v1): Standardized methods for calculating tropical-width diagnostics. *Geoscientific Model Development Discussions*, 11(10), 4339–4357. <https://doi.org/10.5194/gmd-11-4339-2018>
- Afargan, H., & Kaspi, Y. (2017). A midwinter minimum in North Atlantic storm track intensity in years of a strong jet. *Geophysical Research Letters*, 44, 12511–12518. <https://doi.org/10.1002/2017GL075136>
- Allen, R. J., & Kovilakam, M. (2017). The role of natural climate variability in recent tropical expansion. *Journal of Climate*, 30(16), 6329–6350. <https://doi.org/10.1175/JCLI-D-16-0735.1>
- Ambaum, M. H. P., Hoskins, B. J., & Stephenson, D. B. (2001). Arctic oscillation or North Atlantic oscillation? *Journal of Climate*, 14(16), 3495–3507. [https://doi.org/10.1175/1520-0442\(2001\)014<3495:AOONAO>2.0.CO;2](https://doi.org/10.1175/1520-0442(2001)014<3495:AOONAO>2.0.CO;2)
- Archer, C. L., & Caldeira, K. (2008). Historical trends in the jet streams. *Geophysical Research Letters*, 35, L08803. <https://doi.org/10.1029/2008GL033614>
- Athanasiadis, P. J., Wallace, J. M., & Wettstein, J. J. (2010). Patterns of wintertime jet stream variability and their relation to the storm tracks. *Journal of the Atmospheric Sciences*, 67(5), 1361–1381. <https://doi.org/10.1175/2009JAS3270.1>
- Bals-Elsholz, T. M., Atallah, E. H., Bosart, L. F., Wasula, T. A., Cempa, M. J., & Lupo, A. R. (2001). The wintertime Southern Hemisphere split jet: Structure, variability, and evolution. *Journal of Climate*, 14(21), 4191–4215. [https://doi.org/10.1175/1520-0442\(2001\)014<4191:TWSHSJ>2.0.CO;2](https://doi.org/10.1175/1520-0442(2001)014<4191:TWSHSJ>2.0.CO;2)
- Barnes, E. A., & Hartmann, D. L. (2010). Influence of eddy-driven jet latitude on North Atlantic jet persistence and blocking frequency in CMIP3 integrations. *Geophysical Research Letters*, 37, L23802. <https://doi.org/10.1029/2010GL045700>

- Barnes, E. A., & Polvani, L. (2013). Response of the midlatitude jets, and of their variability, to increased greenhouse gases in the CMIP5 models. *Journal of Climate*, 26(18), 7117–7135. <https://doi.org/10.1175/JCLI-D-12-00536.1>
- Brayshaw, D. J., Hoskins, B., & Blackburn, M. (2008). The storm-track response to idealized SST perturbations in an aquaplanet GCM. *Journal of the Atmospheric Sciences*, 65(9), 2842–2860. <https://doi.org/10.1175/2008JAS2657.1>
- Capotondi, A., Wittenberg, A. T., Newman, M., Di Lorenzo, E., Yu, J. Y., Bracchetti, P., et al. (2015). Understanding ENSO diversity. *Bulletin of the American Meteorological Society*, 96(6), 921–938. <https://doi.org/10.1175/BAMS-D-13-00117.1>
- Ceppi, P., & Hartmann, D. L. (2013). On the speed of the eddy-driven jet and the width of the Hadley Cell in the Southern Hemisphere. *Journal of Climate*, 26(10), 3450–3465. <https://doi.org/10.1175/JCLI-D-12-00414.1>
- Choi, J., An, S. I., Kug, J. S., & Yeh, S. W. (2011). The role of mean state on changes in El Niño's flavor. *Climate Dynamics*, 37(5), 1205–1215. <https://doi.org/10.1007/s00382-010-0912-1>
- Christenson, C. E., Martin, J. E., & Handlos, Z. J. (2017). A synoptic climatology of Northern Hemisphere, cold season polar and subtropical jet superposition events. *Journal of Climate*, 30(18), 7231–7246. <https://doi.org/10.1175/JCLI-D-16-0565.1>
- Chung, P. H., & Li, T. (2013). Interdecadal relationship between the mean state and El Niño types. *Journal of Climate*, 26(2), 361–379. <https://doi.org/10.1175/JCLI-D-12-00106.1>
- Cook, A. R., & Schaefer, J. T. (2008). The relation of El Niño–Southern Oscillation (ENSO) to winter tornado outbreaks. *Monthly Weather Review*, 136(8), 3121–3137. <https://doi.org/10.1175/2007MWR2171.1>
- Davis, N., & Birner, T. (2016). Climate model biases in the width of the tropical belt. *Journal of Climate*, 29(5), 1935–1954. <https://doi.org/10.1175/JCLI-D-15-0336.1>
- Davis, N., & Birner, T. (2017). On the discrepancies in tropical belt expansion between reanalyses and climate models and among tropical belt width metrics. *Journal of Climate*, 30(4), 1211–1231. <https://doi.org/10.1175/JCLI-D-16-0371.1>
- Dee, D. P., Uppala, S. M., Simmons, A. J., Berrisford, P., Poli, P., Kobayashi, S., et al. (2011). The ERA-Interim reanalysis: Configuration and performance of the data assimilation system. *Quarterly Journal of the Royal Meteorological Society*, 137(656), 553–597. <https://doi.org/10.1002/qj.828>
- Dickson, R. R., & Namias, J. (1976). North American influences on the circulation and climate of the North Atlantic sector. *Monthly Weather Review*, 104(10), 1255–1265. [https://doi.org/10.1175/1520-0493\(1976\)104<1255:NAIOTC>2.0.CO;2](https://doi.org/10.1175/1520-0493(1976)104<1255:NAIOTC>2.0.CO;2)
- Ding, H., Newman, M., Alexander, M. A., & Wittenberg, A. T. (2020). Relating CMIP5 model biases to seasonal forecast skill in the tropical Pacific. *Geophysical Research Letters*, 47, e2019GL086765. <https://doi.org/10.1029/2019GL086765>
- Eichelberger, S. J., & Hartmann, D. L. (2007). Zonal jet structure and the leading mode of variability. *Journal of Climate*, 20(20), 5149–5163. <https://doi.org/10.1175/JCLI4279.1>
- Eichler, T., & Higgins, W. (2006). Climatology and ENSO-related variability of North American extratropical cyclone activity. *Journal of Climate*, 19(10), 2076–2093. <https://doi.org/10.1175/JCLI3725.1>
- Eyring, V., Bony, S., Meehl, G. A., Senior, C. A., Stevens, B., Stouffer, R. J., & Taylor, K. E. (2016). Overview of the Coupled Model Inter-comparison Project Phase 6 (CMIP6) experimental design and organization. *Geoscientific Model Development*, 9(5), 1937–1958. <https://doi.org/10.5194/gmd-9-1937-2016>
- Gallego, D., Ribera, P., Garcia-Herrera, R., Hernandez, E., & Gimeno, L. (2005). A new look for the Southern Hemisphere jet stream. *Climate Dynamics*, 24(6), 607–621. <https://doi.org/10.1007/s00382-005-0006-7>
- Gillett, Z. E., Hendon, H. H., Arblaster, J. M., & Lim, E. P. (2021). Tropical and extratropical influences on the variability of the Southern Hemisphere wintertime subtropical jet. *Journal of Climate*, 34(10), 4009–4022. <https://doi.org/10.1175/JCLI-D-20-0460.1>
- Greatbatch, R. J., Lu, J., & Peterson, K. A. (2004). Nonstationary impact of ENSO on Euro-Atlantic winter climate. *Geophysical Research Letters*, 31, L02208. <https://doi.org/10.1029/2003GL018542>
- Grise, K. M., Davis, S. M., Staten, P. W., & Adam, O. (2018). Regional and seasonal characteristics of the recent expansion of the tropics. *Journal of Climate*, 31(17), 6839–6856. <https://doi.org/10.1175/JCLI-D-18-0060.1>
- Hall, R., Erdélyi, R., Hanna, E., Jones, J. M., & Scaife, A. A. (2015). Drivers of North Atlantic polar front jet stream variability. *International Journal of Climatology*, 35(8), 1697–1720. <https://doi.org/10.1002/joc.4121>
- Halpert, M. S., & Ropelewski, C. F. (1992). Surface temperature patterns associated with the Southern Oscillation. *Journal of Climate*, 5(6), 577–593. [https://doi.org/10.1175/1520-0442\(1992\)005<0577:STPAWT>2.0.CO;2](https://doi.org/10.1175/1520-0442(1992)005<0577:STPAWT>2.0.CO;2)
- Handlos, Z. J., & Martin, J. E. (2016). Composite analysis of large-scale environments conducive to western Pacific polar/subtropical jet superposition. *Journal of Climate*, 29(19), 7145–7165. <https://doi.org/10.1175/JCLI-D-16-0044.1>
- Held, I. M. (1975). Momentum transport by quasi-geostrophic eddies. *Journal of the Atmospheric Sciences*, 32(7), 1494–1497. [https://doi.org/10.1175/1520-0469\(1975\)032<1494:MTBQGE>2.0.CO;2](https://doi.org/10.1175/1520-0469(1975)032<1494:MTBQGE>2.0.CO;2)
- Held, I. M., & Hou, A. Y. (1980). Nonlinear axially symmetric circulations in a nearly inviscid atmosphere. *Journal of the Atmospheric Sciences*, 37(3), 515–533. [https://doi.org/10.1175/1520-0469\(1980\)037<0515:NASCIA>2.0.CO;2](https://doi.org/10.1175/1520-0469(1980)037<0515:NASCIA>2.0.CO;2)
- Hurrell, J. W. (1995). Decadal trends in the North Atlantic oscillation: Regional temperatures and precipitation. *Science*, 269(5224), 676–679. <https://doi.org/10.1126/science.269.5224.676>
- Jiménez-Esteve, B., & Domeisen, D. I. V. (2018). The tropospheric pathway of the ENSO–North Atlantic teleconnection. *Journal of Climate*, 31(11), 4563–4584. <https://doi.org/10.1175/JCLI-D-17-0716.1>
- Kaas, E., & Branstator, G. (1993). The relationship between a zonal index and blocking activity. *Journal of the Atmospheric Sciences*, 50(18), 3061–3077. [https://doi.org/10.1175/1520-0469\(1993\)050<3061:TRBAZI>2.0.CO;2](https://doi.org/10.1175/1520-0469(1993)050<3061:TRBAZI>2.0.CO;2)
- Kim, H. K., & Lee, S. (2004). The wave-zonal mean flow interaction in the Southern Hemisphere. *Journal of the Atmospheric Sciences*, 61(9), 1055–1067. [https://doi.org/10.1175/1520-0469\(2004\)061<1055:TWMFI>2.0.CO;2](https://doi.org/10.1175/1520-0469(2004)061<1055:TWMFI>2.0.CO;2)
- Koch, P., Wernli, H., & Davies, H. C. (2006). An event-based jet-stream climatology and typology. *International Journal of Climatology*, 26(3), 283–301. <https://doi.org/10.1002/joc.1255>
- Lee, S., & Kim, H. K. (2003). The dynamical relationship between subtropical and eddy-driven jets. *Journal of the Atmospheric Sciences*, 60(12), 1490–1503. [https://doi.org/10.1175/1520-0469\(2003\)060<1490:TDRBSA>2.0.CO;2](https://doi.org/10.1175/1520-0469(2003)060<1490:TDRBSA>2.0.CO;2)
- Li, C., & Wettstein, J. J. (2012). Thermally driven and eddy-driven jet variability in reanalysis. *Journal of Climate*, 25(5), 1587–1596. <https://doi.org/10.1175/JCLI-D-11-00145.1>
- Li, G., & Xie, S. P. (2014). Tropical biases in CMIP5 multimodel ensemble: The excessive equatorial pacific cold tongue and double ITCZ problems. *Journal of Climate*, 27(4), 1765–1780. <https://doi.org/10.1175/JCLI-D-13-00337.1>
- Liebmann, B., & Smith, C. A. (1996). Description of a complete (interpolated) outgoing longwave radiation dataset. *Bulletin of the American Meteorological Society*, 77, 1275–1277.
- Lin, J. L. (2007). The double-ITCZ problem in IPCC AR4 coupled GCMs: Ocean–atmosphere feedback analysis. *Journal of Climate*, 20(18), 4497–4525. <https://doi.org/10.1175/JCLI4272.1>

- Lu, J., Chen, G., & Frierson, D. M. W. (2008). Response of the zonal mean atmospheric circulation to El Niño versus global warming. *Journal of Climate*, 21(22), 5835–5851. <https://doi.org/10.1175/2008JCLI2200.1>
- Maher, P., Kelleher, M. E., Sansom, P. G., & Methven, J. (2020). Is the subtropical jet shifting poleward? *Climate Dynamics*, 54(3–4), 1741–1759. <https://doi.org/10.1007/s00382-019-05084-6>
- Mahlstein, I., Martius, O., Chevalier, C., & Ginsbourger, D. (2012). Changes in the odds of extreme events in the Atlantic basin depending on the position of the extratropical jet. *Geophysical Research Letters*, 39, L22805. <https://doi.org/10.1029/2012GL053993>
- Manney, G. L., & Hegglin, M. I. (2018). Seasonal and regional variations of long-term changes in upper-tropospheric jets from reanalyses. *Journal of Climate*, 31(1), 423–448. <https://doi.org/10.1175/JCLI-D-17-0303.1>
- Menzel, M. E., Waugh, D., & Grise, K. (2019). Disconnect between Hadley Cell and subtropical jet variability and response to increased CO₂. *Geophysical Research Letters*, 46, 7045–7053. <https://doi.org/10.1029/2019GL083345>
- Nakamura, H. (1992). Midwinter suppression of baroclinic wave activity in the Pacific. *Journal of the Atmospheric Sciences*, 49(17), 1629–1642. [https://doi.org/10.1175/1520-0469\(1992\)049<1629:MSOBWA>2.0.CO;2](https://doi.org/10.1175/1520-0469(1992)049<1629:MSOBWA>2.0.CO;2)
- Novak, L., Schneider, T., & Ait-Chaalal, F. (2020). Midwinter suppression of storm tracks in an idealized zonally symmetric setting. *Journal of the Atmospheric Sciences*, 77(1), 297–313. <https://doi.org/10.1175/JAS-D-18-0353.1>
- Panetta, R. L. (1993). Zonal jets in wide baroclinically unstable regions: Persistence and scale selection. *Journal of the Atmospheric Sciences*, 50(14), 2073–2106. [https://doi.org/10.1175/1520-0469\(1993\)050<2073:ZJIWBU>2.0.CO;2](https://doi.org/10.1175/1520-0469(1993)050<2073:ZJIWBU>2.0.CO;2)
- Petoukhov, V., Rahmstorf, S., Petri, S., & Schellnhuber, H. J. (2013). Quasiresonant amplification of planetary waves and recent Northern Hemisphere weather extremes. *Proceedings of the National Academy of Sciences of the United States of America*, 110(14), 5336–5341. <https://doi.org/10.1073/pnas.1222000110>
- Rodionov, S., & Assel, R. (2001). A new look at the Pacific/North American index. *Geophysical Research Letters*, 28(8), 1519–1522. <https://doi.org/10.1029/2000GL012185>
- Ropelewski, C. F., & Halpert, M. S. (1989). Precipitation patterns associated with the high index phase of the southern oscillation. *Journal of Climate*, 2(3), 268–284. [https://doi.org/10.1175/1520-0442\(1989\)002<0268:PPAWTH>2.0.CO;2](https://doi.org/10.1175/1520-0442(1989)002<0268:PPAWTH>2.0.CO;2)
- Ryoo, J. M., Kaspi, Y., Waugh, D. W., Kiladis, G. N., Waliser, D. E., Fetzer, E. J., & Kim, J. (2013). Impact of Rossby wave breaking on U.S. west coast winter precipitation during ENSO events. *Journal of Climate*, 26(17), 6360–6382. <https://doi.org/10.1175/JCLI-D-12-00297.1>
- Sampe, T., Nakamura, H., Goto, A., & Ohfuchi, W. (2010). Significance of a midlatitude SST frontal zone in the formation of a storm track and an eddy-driven westerly jet. *Journal of Climate*, 23(7), 1793–1814. <https://doi.org/10.1175/2009JCLI3163.1>
- Schneider, E. K. (1977). Axially symmetric steady-state models of the basic state for instability and climate studies. Part II. Nonlinear calculations. *Journal of the Atmospheric Sciences*, 34(2), 280–296. [https://doi.org/10.1175/1520-0469\(1977\)034<0280:ASSSMO>2.0.CO;2](https://doi.org/10.1175/1520-0469(1977)034<0280:ASSSMO>2.0.CO;2)
- Seager, R., Murtugudde, R., Naik, N., Clement, A., Gordon, N., & Miller, J. (2003). Air-sea interaction and the seasonal cycle of the subtropical anticyclones. *Journal of Climate*, 16(12), 1948–1966. [https://doi.org/10.1175/1520-0442\(2003\)016<1948:AIATSC>2.0.CO;2](https://doi.org/10.1175/1520-0442(2003)016<1948:AIATSC>2.0.CO;2)
- Smith, S. R., Green, P. M., Leonardi, A. P., & O'Brien, J. J. (1998). Role of multiple-level tropospheric circulations in forcing ENSO winter precipitation anomalies. *Monthly Weather Review*, 126(12), 3102–3116. [https://doi.org/10.1175/1520-0493\(1998\)126<3102:ROMLTC>2.0.CO;2](https://doi.org/10.1175/1520-0493(1998)126<3102:ROMLTC>2.0.CO;2)
- Solomon, A., Polvani, L. M., Waugh, D. W., & Davis, S. M. (2016). Contrasting upper and lower atmospheric metrics of tropical expansion in the Southern Hemisphere. *Geophysical Research Letters*, 43, 10496–10503. <https://doi.org/10.1002/2016GL070917>
- Son, S. W., & Lee, S. (2005). The response of westerly jets to thermal driving in a primitive equation model. *Journal of the Atmospheric Sciences*, 62(10), 3741–3757. <https://doi.org/10.1175/JAS3571.1>
- Strong, C., & Davis, R. E. (2007). Winter jet stream trends over the Northern Hemisphere. *Quarterly Journal of the Royal Meteorological Society*, 133(629), 2109–2115. <https://doi.org/10.1002/qj.171>
- Strong, C., & Davis, R. E. (2008). Variability in the position and strength of winter jet stream cores related to Northern Hemisphere teleconnections. *Journal of Climate*, 21(3), 584–592. <https://doi.org/10.1175/2007JCLI1723.1>
- Wallace, J. M., & Gutzler, D. S. (1981). Teleconnections in the geopotential height field during the Northern Hemisphere winter. *Monthly Weather Review*, 109(4), 784–812. [https://doi.org/10.1175/1520-0493\(1981\)109<0784:TITGHF>2.0.CO;2](https://doi.org/10.1175/1520-0493(1981)109<0784:TITGHF>2.0.CO;2)
- Waugh, D. W., Grise, K. M., Seviour, W. J. M., Davis, S. M., Davis, N., Adam, O., et al. (2018). Revisiting the relationship among metrics of tropical expansion. *Journal of Climate*, 31(18), 7565–7581. <https://doi.org/10.1175/JCLI-D-18-0108.1>
- Winters, A. C., & Martin, J. E. (2016). Synoptic and mesoscale processes supporting vertical superposition of the polar and subtropical jets in two contrasting cases. *Quarterly Journal of the Royal Meteorological Society*, 142(695), 1133–1149. <https://doi.org/10.1002/qj.2718>
- Woollings, T., Barriopedro, D., Methven, J., Son, S. W., Martius, O., Harvey, B., et al. (2018). Blocking and its response to climate change. *Current Climate Change Reports*, 4(3), 287–300. <https://doi.org/10.1007/s40641-018-0108-z>
- Woollings, T., Czuchnicki, C., & Franzke, C. (2014). Twentieth century North Atlantic jet variability. *Quarterly Journal of the Royal Meteorological Society*, 140(680), 783–791. <https://doi.org/10.1002/qj.2197>
- Woollings, T., Hannachi, A., & Hoskins, B. (2010). Variability of the North Atlantic eddy-driven jet stream. *Quarterly Journal of the Royal Meteorological Society*, 136(649), 856–868. <https://doi.org/10.1002/qj.625>
- Yu, B., & Lin, H. (2019). Modification of the wintertime Pacific–North American pattern related North American climate anomalies by the Asian–Bering–North American teleconnection. *Climate Dynamics*, 53(1–2), 313–328. <https://doi.org/10.1007/s00382-018-4586-4>
- Yuan, J., Feldstein, S. B., Lee, S., & Tan, B. (2011). The relationship between the North Atlantic jet and tropical convection over the Indian and western Pacific Oceans. *Journal of Climate*, 24(23), 6100–6113. <https://doi.org/10.1175/2011JCLI4203.1>
- Yuval, J., Afagan, H., & Kaspi, Y. (2018). The relation between the seasonal changes in jet characteristics and the Pacific midwinter minimum in eddy activity. *Geophysical Research Letters*, 45, 9995–10002. <https://doi.org/10.1029/2018GL078678>
- Yuval, J., & Kaspi, Y. (2018). Eddy sensitivity to jet characteristics. *Journal of the Atmospheric Sciences*, 75(5), 1371–1383. <https://doi.org/10.1175/JAS-D-17-0139.1>
- Zhang, W., & Villarini, G. (2018). Uncovering the role of the East Asian jet stream and heterogeneities in atmospheric rivers affecting the western United States. *Proceedings of the National Academy of Sciences of the United States of America*, 115(5), 891–896. <https://doi.org/10.1073/pnas.1717883115>